# Mathematical Modelling and Numerical Simulation with Applications

Volume 5 Issue 3 *MMNSA - September 2025* 

2025

# Stabilized weak-gradient discontinuous finite elements with optimal error estimates for second-order elliptic PDEs

Aymen Laadhari

Department of Mathematics, College of Computing and Mathematical Sciences, Khalifa University of Science and Technology, P.O. Box: 127788, Abu Dhabi, United Arab Emirates, aymen.laadhari@ku.ac.ae

Follow this and additional works at: https://mmnsa.researchcommons.org/journal

Part of the Computational Engineering Commons, Numerical Analysis and Computation Commons, and the Partial Differential Equations Commons

#### **Recommended Citation**

Laadhari, Aymen (2025) "Stabilized weak-gradient discontinuous finite elements with optimal error estimates for second-order elliptic PDEs," *Mathematical Modelling and Numerical Simulation with Applications*: Vol. 5: Iss. 3, Article 8.

DOI: https://doi.org/10.53391/2791-8564.1007

Available at: https://mmnsa.researchcommons.org/journal/vol5/iss3/8

This Original Research Article is brought to you for free and open access by Mathematical Modelling and Numerical Simulation with Applications. It has been accepted for inclusion in Mathematical Modelling and Numerical Simulation with Applications by an authorized editor of Mathematical Modelling and Numerical Simulation with Applications.



## Mathematical Modelling and Numerical Simulation with Applications 2025, 5(3), 644–680



ISSN Online: 2791-8564 / Open Access https://doi.org/10.53391/2791-8564.1007

RESEARCH PAPER

# Stabilized weak-gradient discontinuous finite elements with optimal error estimates for second-order elliptic PDEs

Aymen Laadhari 1,\*,‡

<sup>1</sup>Department of Mathematics, College of Computing and Mathematical Sciences, Khalifa University of Science and Technology, P.O. Box: 127788, Abu Dhabi, United Arab Emirates (ROR)

#### **Abstract**

This work introduces an accurate finite element approach employing a new stabilized discrete weak gradient, designed for second-order elliptic problems on arbitrary conforming meshes. We formulate the approach within a discontinuous Galerkin framework and derive a consistent and coercive bilinear form. Appropriate error analysis on a model problem confirms optimal convergence. Building on the core analysis, we extend the method to more challenging settings, including time-dependent heterogeneous scenarios and a biophysically realistic optimal-control model of photobleaching in the budding yeast cell. We further illustrate the versatility of the weak-gradient construction by applying it to an unsteady level-set equation relevant to multiphase flow modeling. The implementation supports high-order polynomial spaces, varied boundary conditions, and parallel execution with both direct and iterative linear solvers. Computational results corroborate the theoretical analysis and exhibit optimal convergence.

**Keywords**: Finite element method; discontinuous Galerkin; weak gradient; numerical analysis; error estimates

**AMS 2020 Classification**: 65Mxx; 65N15; 65N30; 35B45

#### 1 Introduction

Designing reliable numerical schemes for partial differential equations remains a very active field of research. Discontinuous Galerkin (DG) methods have achieved notable success across diverse disciplines, offering effective solutions for a wide range of physical problems and applications. Extensive studies have examined the mathematical foundations and numerical properties of DG methods. In what follows, we highlight key contributions and provide a bridge to weak Galerkin (WG) methods. Refer, for example, to [1], which provides a pedagogical introduction to DG

➤ Received: 03.06.2025 ➤ Revised: 07.09.2025 ➤ Accepted: 13.09.2025 ➤ Published: 30.09.2025

1

<sup>\*</sup> Corresponding Author

<sup>‡</sup> aymen.laadhari@ku.ac.ae; laadhari@vision.ee.ethz.ch (Aymen Laadhari)

for elliptic and parabolic equations, and the references cited therein. Moreover, [2] develops the mathematical foundations and analysis of DG across representative model problems, [3] surveys recent developments and applications, and [4] presents a Hybridizable Discontinuous Galerkin (HDG) variant incorporating integral boundary conditions. HDG introduces facet (trace) unknowns and enables local static condensation for efficiency. A defining feature of DG methods is their weak enforcement of continuity via stabilization mechanisms, rather than direct imposition through the function space [2]. In particular, "over-penalized" interior penalty variants use a penalty parameter larger than the standard scaling; this can strengthen stability constants and enables superconvergent gradient recovery [5]. The use of discontinuous piecewise polynomial approximations makes them well-suited for solving problems on general finite element meshes. This perspective-stability via weak enforcement and element-local polynomial flexibility-naturally motivates formulations where differential operators themselves are treated in a weak sense, as in WG methods.

Among its many applications, we refer to developments on biharmonic problems [6], level-set problems [7], elasticity and hyperelasticity [8], the Allen-Cahn equation [9], and mixed weak Galerkin formulations for elliptic problems [10]. For illustration: [6] develops a symmetric interiorpenalty DG scheme for the biharmonic problem on meshes with general polygonal (2D) and polyhedral (3D) elements; by "polygonal/polyhedral meshes" we mean general polytopal elements (polygons in 2D, polyhedra in 3D) beyond standard triangles/quadrilaterals. [7] proposes a DG level-set approach for multi-phase modeling; [8] introduces a penalty-free DG formulation for linear elasticity; and [9] analyzes adaptive DG schemes for the Allen-Cahn equation on polygonal meshes. Additionally, DG methods have been used in computational fluid dynamics and complex flows. Indeed, [11] develops an embedded DG formulation for CFD, using a continuous interior trace space to reduce the globally coupled unknowns. [12] develops a DG strategy for the coupled unsteady Stokes/Cahn-Hilliard system, demonstrating optimal convergence on twophase benchmarks. In addition, [13] proposes an HDG approach for compressible flows. In [14], DG is extended to dynamic linear solid viscoelasticity. For complex flows, [15] provides a focused review of numerical methods for yield-stress (viscoplastic) fluids and discusses algorithms tailored to nonsmooth constitutive behavior. In [16], a DG method is developed for dynamic viscoelasticity using a Crank-Nicolson time integrator. Further applications extend to complex physical phenomena such as earthquake-generated waves [17], simulations of reservoirs [18], and fluid transport in fissure-rich porous matrices [19]. See also general overviews and comparisons for convection-dominated problems [20, 21].

In recent years, weak Galerkin (WG) techniques have undergone significant advancements and have been effectively employed across diverse problem classes [22, 23]. WG introduces weak differential operators acting on discontinuous functions and typically includes a stabilizer to weakly enforce continuity across element interfaces, making the approach naturally compatible with general polytopal meshes. Foundational works introduce the discrete weak gradient for elliptic problems and establish optimal error estimates on arbitrary polytopal meshes [10, 22]. Since then, this approach has gained considerable recognition for its effectiveness in handling diverse applications. It has been widely employed in various fields, including elasticity problems [24, 25], solid mechanics [26, 27], and eigenvalue problems [28]. Additionally, it has been applied to solve the biharmonic equations [29, 30], multiphysics and flow modeling - such as Stokes, Darcy, and Brinkman equations [31] - as well as stochastic equations [32], Maxwell equations [33], elliptic [34] and hyperbolic interface problems [35], among others. In summary, the WG viewpoint complements DG: both accept discontinuities at the discrete level, but WG builds weak derivatives into the operator itself, which is central to our approach.

In classical DG, stability is typically enforced by explicit penalty terms added to the discrete bilinear form to control jumps across interfaces [2]. In the present work, our formulation embeds a single interface stabilizer directly into the definition of the weak gradient operator. This placement preserves consistency and yields the discrete coercivity and boundedness required for the analysis, with a stabilization parameter that can be kept very small-specifically, scaled with the square root of the local element size (see Lemma 3). Existing DG and WG formulations typically realize stabilization at the level of the discrete bilinear form through penalty. Embedding stabilization directly in the weak gradient (at the operator level) is less explored. We formalize this idea, prove discrete coercivity and boundedness, establish convergence, and demonstrate numerical robustness on steady and unsteady model problems. This operator-level stabilization links the DG and WG frameworks discussed above to the present method. The literature on polytopal meshes further includes notable contributions for second-order elliptic equations, such as the interior penalty approach [36] and the conforming DG [37]. These results motivate designs that remain accurate and stable on polytopal partitions, a setting handled naturally by weak-operator formulations.

Accordingly, this paper introduces a discontinuous Galerkin approach built upon a weak formulation of the gradient operator. Concretely, we define a stabilized discrete weak gradient by adding a single interface term at the operator level (Definition 1). This construction ensures a well-posed discrete formulation. We perform rigorous error estimation and convergence analysis, demonstrating optimal convergence on arbitrary quasi-uniform meshes.

The approach is readily extended to time-dependent problems with heterogeneous diffusion. These arise widely, e.g., in engineering mathematics when modeling temperature-dependent diffusivity [38]. Furthermore, we present a framework to efficiently solve heterogeneous diffusion in the endoplasmic reticulum of a budding yeast cell, within an optimal control setting. This biologically relevant test case illustrates how the present method adapts to realistic geometries and spatially varying coefficients. For multiphase-flow modeling, we apply the weak gradient formulation to steady advection-reaction problems and unsteady level-set equations. Appropriate modifications to the discrete bilinear forms are introduced, and we only report preliminary numerical results. Finally, we assess the proposed method through numerical experiments in one, two, and three-dimensional settings with high-order polynomial approximations. The numerical evidence shows accurate solutions and convergence at optimal rates.

The article begins with preliminaries. Section 2 describes the discontinuous WG approach along with its main features. Convergence analysis follows in Section 3. Section 4 outlines the model problems and applications. Numerical experiments are presented in Section 5. Section 6 and Section 7 provide concluding remarks and prospective extensions.

## Terminology and notations

Consider a convex polytopal domain  $\Omega \subset \mathbb{R}^d$  with  $d \geqslant 1$ . Let  $\mathcal{M}_h$  be a matching, shape-regular, and contact-regular mesh of  $\Omega$  [39]. The mesh faces  $\mathscr{E}_h$  are partitioned into interior interfaces  $\mathscr{E}_h^i$  (edges (2D) or planar faces (3D)) and boundary faces  $\mathscr{E}_h^b$  (faces lying on  $\partial\Omega$ ). Each face F is assigned a fixed orientation for its unit normal  $\mathbf{n}_F$ : outward from  $T_1$  if  $F = \partial T_1 \cap \partial T_2$ , and outward from  $\Omega$  if  $F \in \mathscr{E}_h^b$ . For  $T \in \mathcal{M}_h$ , denote by  $\mathbf{n}_T$  its outward unit normal and by  $\mathcal{F}_T$  its set of faces. However,  $\mathcal{T}_F$  represents the elements sharing the face  $F \in \mathscr{E}_h$ . The quantity  $N_{\partial T} := \max \operatorname{card}(\mathcal{F}_T)$  on  $\mathcal{M}_h$  denotes the largest number of faces by element. Local mesh sizes are defined as  $h_T$  for an element T, and  $h_F \leqslant h_T$  for a face F. These sizes are assumed to vary smoothly across neighboring elements, whereas  $h := \max h_T$  over  $\mathcal{M}_h$  denotes the overall mesh size.

For a regular function  $\psi: \Omega \to \mathbb{R}$ , consider an interior face  $F = \partial T_1 \cap \partial T_2 \in \mathscr{E}_h^i$ . Define the average

as  $\{\!\!\{\psi\}\!\!\} = (\psi|_{T_1} + \psi|_{T_2})/2$  and the jump as  $[\![\psi]\!] = \psi|_{T_1} - \psi|_{T_2}$  across F. For boundary faces  $F \in \mathscr{E}_h^b$ , the definitions simplify to  $\{\!\!\{\psi\}\!\!\} = \psi|_{T_1}$  and  $[\!\![\psi]\!\!] = \psi|_{T_1}$ , where  $T_1$  is the element sharing F. These trace operators extend component-wise for vector-valued functions. For  $F \in \mathcal{E}_h^i$ , observe that the term  $\{\!\!\{\psi\}\!\!\} - \psi$  is proportional to the jump  $[\!\![\psi]\!\!]$ , with a proportionality coefficient of  $\pm 1/2$ .

Denote by  $\mathbb{P}_d^k(\mathcal{M}_h)$  the broken *k*-order polynomials on  $\mathcal{M}_h$ , belonging to a family of broken piecewise Hilbert spaces  $H^s(\mathcal{M}_h)$ , with  $\mathbb{P}_d^k(\mathcal{M}_h) \subset H^1(\mathcal{M}_h)$  and

$$\mathbb{P}_d^k(\mathcal{M}_h) = \left\{ \xi \in L^2(\Omega) \text{ s.t. } \xi|_T \in \mathbb{P}_d^k(T), \forall T \in \mathcal{M}_h \right\}.$$

Given a subdomain  $K \subset \Omega$ , we use  $(\cdot, \cdot)_K$  for the standard inner products in  $L^2(K)$  and  $[L^2(K)]^d$ . Norms and semi-norms in  $H^s(K)$  are denoted by  $\|\cdot\|_{s,K}$  and  $|\cdot|_{s,K}$ , respectively; By convention,  $H^0(K)$  is identified with  $L^2(K)$ . Given a set S of elements or faces, the inner product  $(\cdot, \cdot)_S$  sums  $(\cdot,\cdot)_K$  over  $\mathcal{S}$ .

On individual mesh elements or faces K, we introduce the piecewise  $L^2$ -orthogonal projector  $\pi_h^k: L^2(K) \to \mathbb{P}_d^k(K)$ . For boundary faces, this projector is denoted by  $\pi_{h,h}^k$ . The vectorial  $L^2$ -projector onto  $[\mathbb{P}_d^k(K)]^d$ , denoted by  $\pi_h^k$ , acts component-wise on vector fields. On regular polytopal meshes, these projectors exhibit optimal approximation properties in  $\mathbb{P}_d^k(K)$  [40].

## **Governing equations**

The Poisson-Dirichlet problem seeks  $u : \Omega \to \mathbb{R}$  such that

$$-\Delta u = f \qquad \text{in } \Omega, \tag{1}$$

with  $f \in L^2(\Omega)$  and  $u = g \in L^2(\partial\Omega)$  on  $\partial\Omega$ . Well-posedness holds true. The variational formulation involves a coercive bilinear form, with  $u \in W = H^1(\Omega)$  satisfying the prescribed boundary condition.

The finite-dimensional discrete space is defined as  $W_h = \mathbb{P}_d^k(\mathcal{M}_h)$ , with  $k \geqslant 1$ . Furthermore, we assume the regularity  $u \in W_{\star} := W \cap H^2(\mathcal{T}_h)$ , which ensures that both u and  $\nabla u \cdot \mathbf{n}$  are square-integrable on  $\mathcal{E}_h$ . This allows u to be used in the discrete weak formulation. The potential u and its normal diffusive flux satisfy the jump conditions:

$$\llbracket u \rrbracket = 0, \quad \forall F \in \mathscr{E}_h^i,$$
 (2a)

Set  $W_{\star h} := W_{\star} + W_{h}$ . The bilinear form is considered on  $W_{\star h} \times W_{\star h}$ . Unless stated otherwise, all constants are mesh- and h-independent. The notation  $x \leq y$  stands for  $x \leq Cy$  for a generic C > 0. Indexed constants remain fixed throughout.

With this notation in place, the next two sections (Section 2 and Section 3) proceed as follows. We define a discrete weak gradient with a single built-in stabilizer (Definition 1). We establish two basic properties: agreement with the projected classical gradient for regular functions (Lemma 1) and links to the standard gradient locally and globally (Lemma 2). Equipped with this gradient, we construct a consistent discrete form via an interface correction and state the discrete problem. We then define an energy-like norm and prove its equivalence with a mesh-dependent norm (Lemma 3). We also establish discrete coercivity and boundedness (Lemma 4 and Lemma 5). Finally, we conclude with optimal a priori error bounds in suitable norms (Theorem 1 and Theorem 2). Subsequent sections present model problems of increasing complexity and the

corresponding numerical experiments.

## 2 Weak Galerkin finite element approach

Let  $\psi$  be piecewise smooth. The discrete weak gradient  $\nabla_{\omega}\psi \in [\mathbb{P}_d^{\kappa}(\mathcal{M}_h)]^d$  is defined element-wise on each  $T \in \mathcal{M}_h$ , including an interface stabilization controlled by a fixed parameter  $\eta$ .

**Definition 1.** Given  $\psi \in H^1(\mathcal{M}_h)$ , we define  $\nabla_{\omega} \psi \in [\mathbb{P}_d^{\kappa}(\mathcal{M}_h)]^d$  satisfying

$$\int_{T} \boldsymbol{\nabla}_{\omega} \boldsymbol{\psi} \cdot \boldsymbol{\xi}_{h} = -\int_{T} \boldsymbol{\psi} \, \nabla \cdot \boldsymbol{\xi}_{h} + \int_{\partial T} \left( \{\!\!\{\boldsymbol{\psi}\}\!\!\} + \frac{\eta}{h_{T}^{1/2}} \big( \{\!\!\{\boldsymbol{\psi}\}\!\!\} - \boldsymbol{\psi} \big) \right) \, \boldsymbol{\xi}_{h} \cdot \mathbf{n}, \quad \forall \boldsymbol{\xi}_{h} \in [\mathbb{P}_{d}^{\kappa}(\mathcal{M}_{h})]^{d}.$$

The parameter  $\eta$  is mesh-independent and it is sufficient to set it small, as will be stated afterwards. A value  $\eta=1$  is set in practice. The degree  $\kappa:=k+N_{\partial T}-1$  is chosen for analysis, though experiments confirm optimal convergence even with smaller  $\kappa$ . In standard Sobolev spaces, the weak gradient corresponds to the  $L^2$ -projection of the usual distributional gradient, as established below.

**Lemma 1.** For any  $v \in W_h$ , if v is sufficiently regular, namely  $v \in H^1(\Omega)$ , then  $\nabla_{\omega} v = \pi_h^{\kappa} \nabla v$  holds true in  $[L^2(\Omega)]^d$ .

**Proof** Following [2, Lemma 1.23],  $v \in H^1(\Omega)$  if and only if  $\llbracket v \rrbracket = 0$  on  $\mathscr{E}_h^i$ , which implies  $\llbracket v \rrbracket = v$  on  $F \in \mathscr{E}_h^i$ . By applying Definition 1 together with the characterization of the orthogonal projection  $\pi_h^{\kappa}$ , we successively obtain:

$$\begin{aligned} \left( \boldsymbol{\nabla}_{\omega} v, \boldsymbol{\Psi}_{h} \right)_{T} &= - \left( v, \nabla \cdot \boldsymbol{\Psi}_{h} \right)_{T} + \left( v, \boldsymbol{\Psi}_{h} \cdot \mathbf{n} \right)_{\partial T} \\ &= \left( \boldsymbol{\nabla} v, \boldsymbol{\Psi}_{h} \right)_{T} = \left( \boldsymbol{\pi}_{h}^{\kappa} \boldsymbol{\nabla} v, \boldsymbol{\Psi}_{h} \right)_{T}, \qquad \forall \boldsymbol{\Psi}_{h} \in \left[ \mathbb{P}_{d}^{\kappa} (\mathcal{M}_{h}) \right]^{d}. \end{aligned}$$

Since the element  $T \in \mathcal{M}_h$  and the vector field  $\mathbf{\Psi}_h \in [\mathbb{P}_d^{\kappa}(\mathcal{M}_h)]^d$  are arbitrary, we conclude that  $\nabla_{\omega} v = \nabla v = \pi_h^{\kappa} \nabla v$  by choosing  $\mathbf{\Psi}_h = \nabla_{\omega} v - \pi_h^{\kappa} \nabla v \in [\mathbb{P}_d^{\kappa}(\mathcal{M}_h)]^d$ .

The following lemma relates the weak gradient to the usual gradient at the local and global level.

**Lemma 2.** Consider  $v \in W_h$ . For all  $\xi_h \in [\mathbb{P}_d^{\kappa}(\mathcal{M}_h)]^d$ , the following properties hold:

• On each element  $T \in \mathcal{M}_h$ ,

$$\left(\boldsymbol{\nabla}_{\omega}v,\boldsymbol{\xi}_{h}\right)_{T} = \left(\boldsymbol{\nabla}v,\boldsymbol{\xi}_{h}\right)_{T} + \left(\left(1 + \eta h_{T}^{-1/2}\right)\left(\{\!\!\{v\}\!\!\} - v\right),\boldsymbol{\xi}_{h} \cdot \mathbf{n}\right)_{\partial T}, \forall T \in \mathcal{M}_{h}. \tag{3}$$

• Over the entire mesh  $\mathcal{M}_h$ ,

$$\left(\nabla v - \nabla_{\omega} v, \xi_h\right)_{\mathcal{M}_h} = \left(\llbracket v \rrbracket, \left\{ \left\{ \left(1 + \eta h_T^{-1/2}\right) \xi_h \right\} \right\} \cdot \mathbf{n}_F \right)_{\mathcal{E}_h^i}. \tag{4}$$

**Proof** Eq. (3) follows from integration by parts, followed by subtracting (1).

Summing over all elements in  $\mathcal{M}_h$ , Eq. (3) is expressed as sum over  $\mathscr{E}_h$ . We shall separate first the contributions from internal and boundary faces. On internal faces, any scalar-valued functions  $\alpha$  and  $\beta$  satisfy  $[\![\alpha\beta]\!] = [\![\alpha]\!] \{\![\beta]\!] + \{\![\alpha]\!] [\![\beta]\!]$ , as well as  $\{\![\alpha-\{\![\alpha]\!]\}\!] = 0$  and similarly for  $\beta$ .

Taking into account the convension for boundary averages and using the latter properties, we

obtain:

$$\begin{split} &\sum_{T \in \mathcal{M}_h} \left( v - \{\!\!\{ v \}\!\!\}, \left( 1 + \eta h_T^{-1/2} \right) \, \boldsymbol{\xi}_h \cdot \mathbf{n} \right)_{\partial T} \\ &= \sum_{F \in \mathcal{E}_h^b} \left( v - \{\!\!\{ v \}\!\!\}, \left( 1 + \eta h_T^{-1/2} \right) \, \boldsymbol{\xi}_h \cdot \mathbf{n}_F \right)_F + \sum_{F \in \mathcal{E}_h^i} \left( \left[ \left( v - \{\!\!\{ v \}\!\!\}\right) \left( 1 + \eta h_T^{-1/2} \right) \boldsymbol{\xi}_h \right] \right], \mathbf{n}_F \right)_F \\ &= \sum_{F \in \mathcal{E}_h^i} \left( \left[ v - \{\!\!\{ v \}\!\!\}\right], \left\{ \left\{ \left( 1 + \eta h_T^{-1/2} \right) \boldsymbol{\xi}_h \right\} \right\} \cdot \mathbf{n}_F \right)_F \\ &= \sum_{F \in \mathcal{E}_h^i} \left( \left[ v \right], \left\{ \left\{ \left( 1 + \eta h_T^{-1/2} \right) \boldsymbol{\xi}_h \right\} \right\} \cdot \mathbf{n}_F \right)_F. \end{split}$$

As a result, assertion (4) follows.

Under the quasi-uniform mesh assumption, we identify  $\{h_T\}$   $\sim h_T$  on  $\mathcal{E}_h^i$ . The assumption holds naturally in the context of regular, structured meshes. Let  $W_h^0 \subset W_h$  be the subspace of functions with vanishing trace on  $\partial\Omega$ . For  $(v, \xi_h) \in W_{\star h} \times W_h^0$ , define a bilinear form:

$$a_h^{(0)}(v,\xi_h) \coloneqq \sum_{T \in \mathcal{M}_h} \int_T \boldsymbol{\nabla}_{\omega} v \cdot \boldsymbol{\nabla}_{\omega} \xi_h.$$

To analyze consistency, we first perform elementwise integration by parts using (1) and then sum over  $\mathcal{T}_h$ . The initial integral is subsequently integrated by parts. Thus,

$$a_{h}^{(0)}(v,\xi_{h}) = \left(-v,\nabla\cdot\boldsymbol{\nabla}_{\omega}\xi_{h}\right)_{\mathcal{M}_{h}} + \left(\{\{v\}\} + \eta h_{T}^{-1/2}(\{\{v\}\} - v),\boldsymbol{\nabla}_{\omega}\xi_{h}\cdot\mathbf{n}\right)_{\partial\mathcal{M}_{h}}$$
$$= \left(\boldsymbol{\nabla}v,\boldsymbol{\nabla}_{\omega}\xi_{h}\right)_{\mathcal{M}_{h}} + \left(\{\{v\}\} - v,\left(1 + \eta h_{T}^{-1/2}\right)\boldsymbol{\nabla}_{\omega}\xi_{h}\cdot\mathbf{n}\right)_{\partial\mathcal{M}_{h}}.$$

We then use (1) and express the second and third integrals, originally defined over the boundaries of mesh elements, as sums over the mesh faces. The contributions are accordingly separated into internal and boundary face terms. As a result, we obtain

$$a_{h}^{(0)}(v,\xi_{h}) = (-\Delta v,\xi_{h})_{\mathcal{M}_{h}} + \left( \{\xi_{h}\}\} + \frac{\eta}{h_{T}^{1/2}} (\{\xi_{h}\}\} - \xi_{h}), \nabla v \cdot \mathbf{n} \right)_{\partial \mathcal{M}_{h}}$$

$$+ \left( \{v\}\} - v, \left( 1 + \frac{\eta}{h_{T}^{1/2}} \right) \nabla_{\omega} \xi_{h} \cdot \mathbf{n} \right)_{\partial \mathcal{M}_{h}}$$

$$= (-\Delta v, \xi_{h})_{\mathcal{M}_{h}} + (\xi_{h}, \nabla v \cdot \mathbf{n}_{F})_{\mathcal{E}_{h}^{b}} - \left( [\eta h_{T}^{-1/2} \xi_{h}], \{\nabla v\}\} \cdot \mathbf{n}_{F} \right)_{\mathcal{E}_{h}^{i}} + (\{\xi_{h}\}\}, [\nabla v]\} \cdot \mathbf{n}_{F})_{\mathcal{E}_{h}^{i}}$$

$$- \left( \left( 1 + \eta h_{T}^{-1/2} \right) [v], \{\nabla_{\omega} \xi_{h}\}\} \cdot \mathbf{n}_{F} \right)_{\mathcal{E}_{h}^{i}}. \tag{5}$$

Setting v = u and accounting for the continuity of the potential and diffusive flux (2) across  $\mathcal{E}_h^i$ , it is found that the bilinear form  $a_h^{(0)}$  lacks consistency.

To enforce consistency, a corrective term is introduced; this corresponds to the second integral in (6). Similar to the continuous setting, an additional term scaled by  $\delta$  is included, which yields a symmetric bilinear form when  $\delta = 1$ . The parameter  $\delta$  also helps tuning the discrete stability

constant, see Lemma 4. Let  $(v, \xi_h) \in W_{\star h} \times W_h^0$ . Introduce

$$a_h(v,\xi_h) := \sum_{T \in \mathcal{M}_h} \int_T \mathbf{\nabla}_{\omega} v \cdot \mathbf{\nabla}_{\omega} \xi_h + \int_{\mathscr{E}_h^i} \frac{\eta}{h_T^{1/2}} \{\!\{ \mathbf{\nabla} v \}\!\} \cdot \mathbf{n}_F [\![ \xi_h ]\!] + \delta \int_{\mathscr{E}_h^i} \frac{\eta}{h_T^{1/2}} [\![ v ]\!] \{\!\{ \mathbf{\nabla} \xi_h \}\!\} \cdot \mathbf{n}_F. \tag{6}$$

Consistency is preserved by the last term, given the continuity of the potential. Moreover, Galerkin orthogonality holds for all  $\delta \in \mathbb{R}$ . Numerical results presented later demonstrate that optimal convergence is achieved even for the case  $\delta = 0$ . The numerical solution  $u_h \in W_h$  satisfies

$$a_h(u_h, \xi_h) = (f, \xi_h)_{\mathcal{M}_h}, \quad \forall \xi_h \in W_h^0, \tag{7}$$

with  $u_h|_F = \pi_{h,b}^k g$  for all  $F \in \mathcal{E}_h^b$ . For  $v \in W_{\star h}$ , we introduce mesh-dependent discrete seminorms

$$||v||_{\omega}^{2} := a_{h}^{(0)}(v, v),$$

$$||v||_{h,1}^{2} := ||\nabla v||_{0,\mathcal{M}_{h}}^{2} + |v|_{J}^{2}, \quad \text{with} \quad |v|_{J}^{2} := \sum_{F \in \mathscr{E}_{h}} \frac{1}{h_{F}^{2}} ||[v]||_{0,F}^{2}.$$

The norm  $\|\cdot\|_{h,1}$  is well-defined on  $W_{\star h}$ , and also on  $H^1(\mathcal{M}_h)$ . Indeed, the nontrivial definiteness property holds since  $\|v\|_{h,1}=0$  results in  $\|\nabla v\|_{0,T}^2=0$ , so v is piecewise constant by the Poincaré inequality. Additionally,  $|v|_J=0$  implies v=0 on  $\partial\Omega$  and that jumps vanish on internal interfaces, leading to v=0. The following lemma on seminorm equivalence infers that  $\|\cdot\|_{\omega}$  is a norm.

**Lemma 3.** Let  $v \in W_h$ . Assume that  $\eta^2 \geqslant \max_{T \in \mathcal{M}_h} h_T$ . Hence,

$$||v||_{h,1} \lesssim ||v||_{\omega} \lesssim ||v||_{h,1},$$

establishing norm equivalence.

**Proof** Consider general polytopal meshes. Norm equivalence is established using [37, Lemma 3.1].

First, we demonstrate the upper bound. Eq. (8) follows by taking  $\xi_h = \nabla_\omega v$  in (4), then applying the triangle inequality and noting  $h_F \leq h_T$ .

Summing over  $\mathcal{E}_h$  and applying Cauchy-Schwarz, we obtain (9) after reorganizing the terms elementwise. The upper bound is then derived via the trace inequality with the constant  $C_{tr}$ . Hence,

$$\|v\|_{\omega}^{2} := \|\nabla_{\omega}v\|_{0,\mathcal{M}_{h}}^{2}$$

$$\leq \left|\sum_{T \in \mathcal{M}_{h}} (\nabla_{\omega}v, \nabla v)_{T}\right| + \left|\sum_{F \in \mathcal{E}_{h}^{i}} 2\frac{\eta}{h_{F}} \|[v]\|_{0,F} \cdot h_{F}^{1/2} \|\nabla_{\omega}v\|_{0,F}\right|$$

$$\leq \|\nabla_{\omega}v\|_{0,\mathcal{M}_{h}} \|\nabla v\|_{0,\mathcal{M}_{h}} + 2\eta \left(\sum_{F \in \mathcal{E}_{h}^{i}} h_{F}^{-2} \|[v]\|_{0,F}^{2}\right)^{1/2} \left(\sum_{T \in \mathcal{M}_{h}} \sum_{F \in \mathcal{F}_{T}} h_{F} \|\nabla_{\omega}v\|_{0,F}^{2}\right)^{1/2}$$
(9)

$$\leq \|v\|_{\omega} \|\nabla v\|_{0,\mathcal{M}_{h}} + 2\eta \|v\|_{J} \left( \sum_{T \in \mathcal{M}_{h}} h_{T} \|\nabla_{\omega}v\|_{0,\partial T}^{2} \right)^{1/2} \\
\leq \left( 1 + 2\eta C_{\text{tr}} N_{\partial T}^{1/2} \right) \|v\|_{\omega} \|v\|_{h,1}. \tag{10}$$

Accordingly, the required upper bound holds.

Next, we derive a lower bound. Choosing  $\xi_h = \nabla v$  in (3) and summing over  $\mathcal{M}_h$ , we successively use the triangle, Cauchy-Schwarz and discrete trace inequalities to derive:

$$\begin{split} \|\nabla v\|_{0,\mathcal{M}_{h}}^{2} & \leq \sum_{T \in \mathcal{M}_{h}} \|\nabla_{\omega}v\|_{0,T} \|\nabla v\|_{0,T} + \left| \sum_{T \in \mathcal{M}_{h}} \left( \frac{1}{h_{T}^{1/2}} \left( 1 + \frac{\eta}{h_{T}^{1/2}} \right) (\{v\} - v), h_{T}^{1/2} \nabla v \cdot \mathbf{n} \right)_{\partial T} \right| \\ & \leq \|\nabla_{\omega}v\|_{0,\mathcal{M}_{h}} \|\nabla v\|_{0,\mathcal{M}_{h}} \\ & + N_{\partial T}^{1/2} \bar{C}_{tr} \left( \sum_{T \in \mathcal{M}_{h}} \|\nabla v\|_{0,\mathcal{M}_{h}} \left( h_{T}^{-1/2} \left( 1 + \eta h_{T}^{-1/2} \right) \|\{v\} - v\|_{0,\partial T} \right)^{2} \right)^{1/2}. \end{split}$$

We then need to bound the second term. Let  $F \in \mathcal{E}_h^i$  and  $T \in \mathcal{T}_F$ . Assume  $n_1 \neq 0$ , with  $n_i$   $(1 \leq i \leq d)$  the components of  $\mathbf{n}_F$  (otherwise, the first nonzero component of  $\mathbf{n}_F$  is used instead of  $n_1$ ). Define  $q_0 := \{\{v\}\} - v \in \mathbb{P}_d^k(F)$ .

By [37, Lemma 3.1], there exists  $q \in \mathbb{P}_d^{\kappa}(T)$ , with  $\kappa = k + N_{\partial T} - 1$ , satisfying the properties [37, (18)-(20)]. We define  $\tilde{\boldsymbol{\xi}} \in [\mathbb{P}_d^{\kappa}(T)]^d$  such that its first component is  $q/n_1$ , with all others zero. This ensures  $\tilde{\boldsymbol{\xi}} \cdot \mathbf{n}_F = q$ . Let  $p = (1 + \eta h_T^{-1/2})(\{\{v\}\} - v) \in \mathbb{P}_d^k(F)$ . Owing to [37, (18)], we infer:

$$\left( \left( 1 + \eta h_T^{-1/2} \right) \left( \{ \{ v \} \} - v \right), \tilde{\xi} \cdot \mathbf{n}_F \right)_F := (p, q)_F = (p, q_0)_F = \left( 1 + \eta h_T^{-1/2} \right) \left\| \{ \{ v \} \} - v \right\|_{0,F}^2, \qquad (11a)$$

$$\left( \nabla v, \tilde{\xi} \right)_T = 0, \text{ and } \left( \left( 1 + \eta h_T^{-1/2} \right) \left( \{ \{ v \} \} - v \right), \tilde{\xi} \cdot \mathbf{n}_F \right)_{\partial T \setminus F} = 0. \qquad (11b)$$

Here,  $h_T \le 4h_F$  was assumed. Using [37, (26)] and (11), a constant  $C_{\alpha_0} > 0$ , that depends on k,  $N_{\partial T}$ , and the smallest angle between F and its adjacent faces, exists such that:

$$\|\tilde{\xi}\|_{0,T} \leqslant C_{\alpha_0} h_T^{1/2} \|q_0\|_{0,F} = C_{\alpha_0} h_T^{1/2} \|\{v\} - v\|_{0,F}.$$

Using the identity  $\|[v]\|_{0,F} = 2 \|\{v\} - v\|_{0,F}$ , valid over internal faces  $\mathcal{E}_h^i$ , we proceed as follows. With  $\xi_h = \tilde{\xi}$  in (3), we obtain by Cauchy-Schwarz

$$\left(1 + \eta h_T^{-1/2}\right) \| [v] \|_{0,F} \leqslant 2 \left(1 + \eta h_T^{-1/2}\right) \| \{v\} - v\|_{0,F} \leqslant 2C_{\alpha_0} h_T^{1/2} \| \boldsymbol{\nabla}_{\omega} v\|_{0,T}.$$
 (12)

Using (12) and summing over  $\mathcal{E}_h$ , we obtain:

$$\|\boldsymbol{\nabla}v\|_{0,\mathcal{M}_h} \leqslant \left(1 + N_{\partial T}^{1/2} C_{\alpha_0} \bar{C}_{tr}\right) \|v\|_{\omega}. \tag{13}$$

Using the first inequality in (12) with  $h_T \leq 4h_F$  and collecting the contributions over all faces

$$\eta |v|_{\mathsf{I}} \leqslant 8C_{\alpha_0} \|v\|_{\alpha}.$$
 (14)

Together with (13), we derive the upper estimate:

$$||v||_{\mathsf{h},1} \leqslant C_{\omega} |||v||_{\omega},$$
 (15)

with

$$C_{\omega}^{2} = (8\eta^{-1}C_{\alpha_{0}})^{2} + (1 + C_{\alpha_{0}}N_{\partial T}^{1/2}\bar{C}_{tr})^{2} \geqslant 1.$$

Collecting (10) and (15), we obtain the desired double inequality:

$$C_{\omega}^{-1} \|v\|_{\mathrm{h},1} \leqslant \|v\|_{\omega} \leqslant \left(1 + 2\eta \ N_{\partial T}^{1/2} \ C_{\mathrm{tr}}\right) \ \|v\|_{\mathrm{h},1}.$$

## 3 Convergence analysis

Let  $\phi_{\pi} \coloneqq u - \pi_h^k u$  and  $\phi_h \coloneqq \pi_h^k u - u_h$ , allowing the approximation error to be decomposed as  $u - u_h = \phi_{\pi} + \phi_h$ . We aim to establish error estimates in  $\|\cdot\|_{\omega}$  and  $L^2$  norms.

**Lemma 4.** (Discrete stability) Discrete coercivity of  $a_h$  over  $W_h$  holds in the  $\|\cdot\|_{\omega}$ -norm, provided that  $|\delta+1|<\bar{\delta}$ , with  $\bar{\delta}$  a threshold value independent of h. That is, there exists  $C_s>0$  s.t.

$$a_h(\psi_h,\psi_h)\geqslant C_s \|\psi_h\|_{\omega}^2, \quad \forall \psi_h\in W_h.$$

**Proof** To establish discrete coercivity, we first bound the consistency term in (6). As in (9), we use  $h_F \leq h_T$ , then apply Cauchy–Schwarz and trace inequality, involving constants  $\bar{C}_{tr}$  and  $N_{\partial T}$ . For any  $\psi_h \in W_h$ , we obtain

$$\left| \sum_{F \in \mathcal{E}_{h}^{i}} \int_{F} h_{T}^{-1/2} \{\!\!\{ \nabla \psi_{h} \}\!\!\} \cdot \mathbf{n}_{F} [\!\![ \psi_{h} ]\!\!] \right| \leq \left( \sum_{F \in \mathcal{E}_{h}^{i}} h_{F}^{-2} \| [\!\![ \psi_{h} ]\!\!] \|_{0,F}^{2} \right)^{1/2} \left( \sum_{T \in \mathcal{M}_{h}} \sum_{F \in \mathcal{F}_{T}} h_{F} \| \nabla \psi_{h} \|_{1,F} \cdot \mathbf{n}_{F} \|_{0,F}^{2} \right)^{1/2}$$

$$\leq \| \psi_{h} \|_{J} \left( \sum_{T \in \mathcal{M}_{h}} h_{T} \| \nabla \psi_{h} \|_{0,\partial T}^{2} \right)^{1/2}$$

$$\leq N_{\partial T}^{1/2} \bar{C}_{tr} \| \nabla \psi_{h} \|_{0,\mathcal{M}_{h}} |\psi_{h}|_{J}$$

$$\leq 8C_{\alpha_{0}} \eta^{-1} N_{\partial T}^{1/2} \bar{C}_{tr} \left( 1 + C_{\alpha_{0}} \bar{C}_{tr} N_{\partial T}^{1/2} \right) \| \psi_{h} \|_{\omega}^{2} . \tag{16}$$

The last inequality (16) results from the bounds on  $\|\nabla \psi_h\|_{0,\mathcal{M}_h}$  (13) and  $|\psi_h|_{\mathbb{T}}$  (14). Then,

$$\begin{split} a_h(\psi_h,\psi_h) &= & \left\|\psi_h\right\|_\omega^2 + \eta\left(1+\delta\right) \sum_{F \in \mathscr{E}_h^i} \int_F \frac{1}{h_T^{1/2}} \left\|\nabla \psi_h\right\| \cdot \mathbf{n}_F \left[\!\left[\psi_h\right]\!\right] \geqslant C_\mathrm{s} \left\|\psi_h\right\|_\omega^2, \\ \text{with} & C_\mathrm{s} := 1 - 8 \left|1 + \delta\right| C_{\alpha_0} N_{\partial T}^{1/2} \bar{C}_\mathrm{tr} \left(1 + C_{\alpha_0} N_{\partial T}^{1/2} \bar{C}_\mathrm{tr}\right) > 0, \end{split}$$

provided that  $|\delta+1| < \bar{\delta}$  with  $\bar{\delta}^{-1} \coloneqq 8C_{\alpha_0}N_{\partial T}^{1/2}\bar{C}_{tr}(1+C_{\alpha_0}N_{\partial T}^{1/2}\bar{C}_{tr})$ . Therefore, by Lax–Milgram, (7) is well-posed.

**Lemma 5.** The bilinear form is bounded on  $W_{\star h} \times W_h$ :

$$\left| a_h(v, \xi_h) \right| \leqslant C_b \left\| v \right\|_{\omega} \left\| \xi_h \right\|_{\omega}, \qquad \forall v \in W_{\star h}, \, \forall \xi_h \in W_h, \tag{17}$$

with  $C_b > 0$  a mesh-independent constant.

**Proof** For  $v \in W_{\star h}$  and  $\xi_h \in W_h$ , the triangle inequality helps bounding the terms in  $a_h$ . Summing over faces, applying Cauchy–Schwarz, and regrouping contributions of  $\mathcal{E}_h$  yields (18a). In addition, the discrete trace inequality with constant  $\bar{C}_{tr}$  gives (18b), while bounds (13) and (15) lead to (18c). Thus, we have

$$|a_{h}(v,\xi_{h})| \leq \|\nabla_{\omega}v\|_{0,\mathcal{M}_{h}} \|\nabla_{\omega}\xi_{h}\|_{0,\mathcal{M}_{h}} + \eta \left(\sum_{T \in \mathcal{M}_{h}} \sum_{F \in \mathcal{F}_{T}} h_{T} \|\nabla\psi_{h}\|_{0,\partial T}^{2}\right)^{1/2} |\xi_{h}|_{J} + |\delta| \eta |v|_{J} \left(\sum_{T \in \mathcal{M}_{h}} \sum_{F \in \mathcal{F}_{T}} h_{T} \|\nabla\xi_{h}\|_{0,\partial T}^{2}\right)^{1/2}$$

$$\leq \|v\|_{\omega} \|\xi_{h}\|_{\omega} + N_{\partial T}^{1/2} \bar{C}_{tr} \|\nabla v\|_{0,\mathcal{M}_{h}} \eta |\xi_{h}|_{J} + |\delta| N_{\partial T}^{1/2} \bar{C}_{tr} \eta |v|_{J} \|\nabla\xi_{h}\|_{0,\mathcal{M}_{h}}$$

$$\leq \|v\|_{\omega} \|\xi_{h}\|_{\omega} + 8C_{\alpha_{0}} N_{\partial T}^{1/2} \bar{C}_{tr} (1 + |\delta|) \left(1 + C_{\alpha_{0}} N_{\partial T}^{1/2} \bar{C}_{tr}\right) \|v\|_{\omega} \|\xi_{h}\|_{\omega}$$

$$\leq \|1 + 8(1 + |\delta|) C_{\alpha_{0}} N_{\partial T}^{1/2} \bar{C}_{tr} \left(1 + C_{\alpha_{0}} \bar{C}_{tr} N_{\partial T}^{1/2}\right) \|v\|_{\omega} \|\xi_{h}\|_{\omega}$$

$$\leq (1 + 8(1 + |\delta|) C_{\alpha_{0}} N_{\partial T}^{1/2} \bar{C}_{tr} \left(1 + C_{\alpha_{0}} \bar{C}_{tr} N_{\partial T}^{1/2}\right) \|v\|_{\omega} \|\xi_{h}\|_{\omega} .$$

$$(18d)$$

$$\leqslant \left(1 + 8(1 + |\delta|)C_{\alpha_0}N_{\partial T}^{1/2}\bar{C}_{tr}\left(1 + C_{\alpha_0}\bar{C}_{tr}N_{\partial T}^{1/2}\right)\right) |\!|\!|v|\!|\!|_{\omega} |\!|\!|\xi_h|\!|\!|_{\omega}.$$
(18d)

From (18d), the desired boundedness (17) then holds with

$$C_b = 1 + 8 \left( 1 + |\delta| \right) C_{\alpha_0} N_{\partial T}^{1/2} \bar{C}_{tr} \left( 1 + C_{\alpha_0} N_{\partial T}^{1/2} \bar{C}_{tr} \right),$$

which is independent of h and  $\eta$ .

**Lemma 6.** Assume sufficient regularity with  $u \in H^{k+1}(\Omega)$ . Consider a quasi-uniform mesh with optimal polynomial approximation properties and h sufficiently small. Then,

$$\|\phi_{\pi}\|_{\omega} \lesssim h^k |u|_{k+1,\Omega}. \tag{19}$$

**Proof** For  $T \in \mathcal{M}_h$ , we use (3) and the triangle inequality in (20a). Note that  $\{u\} = u$ , so  $[\![\pi_h^k u]\!] = [\![-\phi_\pi]\!]$  on  $\mathscr{E}_h$ . The Cauchy-Schwarz and trace inequalities yield (20b), while (12) and the inverse inequality lead to (20c). Hence,

$$\begin{aligned}
\left| \left( \nabla_{\omega} \phi_{\pi}, \xi_{h} \right)_{T} \right| &\leq \left| \left( \nabla \phi_{\pi}, \xi_{h} \right)_{T} \right| + \left| \left( h_{T}^{-1/2} \left( 1 + \eta h_{T}^{-1/2} \right) \left( \left\{ \phi_{\pi} \right\} - \phi_{\pi} \right), h_{T}^{1/2} \xi_{h} \cdot \mathbf{n} \right)_{\partial T} \right| & (20a) \\
&\leq \left| \left| \nabla \left( u - \pi_{h}^{k} u \right) \right|_{0,T} \|\xi_{h}\|_{0,T} \\
&+ (1/2) C_{\text{tr}} N_{\partial T}^{1/2} h_{T}^{-1/2} \left( 1 + \eta h_{T}^{-1/2} \right) \| \left[ \pi_{h}^{k} u \right] \|_{0,\partial T} \|\xi_{h}\|_{0,T} & (20b)
\end{aligned}$$

$$\leq \bar{C} h^k |u|_{k+1,T} \|\xi_h\|_{0,T} + C \|\nabla_\omega \phi_\pi\|_{0,T} \|\xi_h\|_{0,T}.$$
 (20c)

Here, C > 0 is determined solely by  $C_{\alpha_0}$ ,  $N_{\partial T}$  and  $C_{\rm tr}$  (trace inequality constant). Letting  $\xi_h = \nabla_\omega \phi_\pi$  and summing over mesh elements, the bound (19) holds provided C < 1, using the identity  $\| \llbracket \pi_h^k u \rrbracket \|_{0,\partial T} = \| \llbracket \phi_\pi \rrbracket \|_{0,\partial T}$  in (20b). Alternatively, for sufficiently smooth u and large k, the projection  $\pi_h^k u$  adequately captures the smoothness of u, yielding near-continuity across  $\mathcal{E}_h^i$ . When h is small, intra-element variations in u and its derivatives are reduced, minimizing interface jumps. Quasi-uniformity of the mesh ensures geometric regularity and prevents excessive contributions of individual elements. Thus, the first term in (20b) dominates, and the bound scales as  $h^k$ .

Remark that if neither of the two aforementioned conditions are satisfied, then, by the trace inequality, the second term in (20b) dominates and results in a quasi-optimal convergence in  $\|.\|_{\omega}$ . That will result subsequently in a suboptimal decay  $h^{k+\frac{1}{2}}$  for the  $L^2$ -error.

**Theorem 1** ( $\|\cdot\|_{\omega}$ -error bound). Assume the conditions of Lemma 6. Let  $u \in W_{\star}$  solve (1), and let  $u_h \in W_h$  solve (7). There holds

$$|||u - u_h||_{\omega} \lesssim h^k |u|_{k+1,\Omega}. \tag{21}$$

**Proof** Using the triangle inequality, as well as the stability, consistency, and boundedness properties, we deduce the estimate:

$$\begin{split} \| u - u_h \|_{\omega} & \leqslant & \| \phi_{\pi} \|_{\omega} + \| \phi_h \|_{\omega} \\ & \leqslant & \| \phi_{\pi} \|_{\omega} + \frac{1}{C_s} \frac{a_h(\phi_h, \phi_h)}{\| \phi_h \|_{\omega}} \\ & \leqslant & \| \phi_{\pi} \|_{\omega} + \frac{1}{C_s} \frac{|a_h(\phi_{\pi}, \phi_h)|}{\| \phi_h \|_{\omega}} \\ & \leqslant & \left( 1 + \frac{C_b}{C_s} \right) \| \phi_{\pi} \|_{\omega} \,. \end{split}$$

The latter bound is valid for  $u_h = \pi_h^k u$ . The estimate (21) results from Lemma 6.

**Theorem 2** ( $\|\cdot\|_{0,\Omega}$ -error bound). *Assuming the conditions of Lemma 6*, *elliptic regularity, and setting*  $\delta = 1$ , we obtain the estimate:

$$||u - u_h||_{0,\Omega} \lesssim h^{k+1} |u|_{k+1,\Omega}.$$
 (22)

**Proof** A duality argument is used after extending  $a_h$  to  $W_{\star h} \times W_{\star h}$ . The symmetry of  $a_h$  enables using the Aubin–Nitsche technique [41]. Let  $\Psi \in H_0^2(\Omega)$  solve the auxiliary problem:

$$-\Delta \Psi = u - u_h = \phi_{\pi} + \phi_h$$
.

Elliptic regularity ensures the existence of  $C_{\Omega} > 0$ , depending solely on  $\Omega$ , s.t.

$$\|\Psi\|_{2,\Omega} \leqslant C_{\Omega} \|\phi_{\pi} + \phi_h\|_{0,\Omega}.$$

Remark that  $a_h(\phi_\pi + \phi_h, \pi_h^1 \Psi)$  vanishes by Galerkin orthogonality. Exploiting the symmetry of  $a_h$ ,

this gives

$$\|u-u_h\|_{0,\Omega}^2 = a_h(\Psi,\phi_\pi+\phi_h) = a_h(\phi_\pi+\phi_h,\Psi) = a_h(\phi_\pi+\phi_h,\Psi-\pi_h^1\Psi).$$

Using Lemma 5, the approximation properties for  $\pi_h^1$ , and elliptic regularity, we infer:

$$\|u - u_h\|_{0,\Omega}^2 \lesssim \| \|\Psi - \pi_h^1 \Psi \|_{\omega} \| \phi_{\pi} + \phi_h \|_{\omega}$$

$$\lesssim h \|\Psi\|_{2,\Omega} \| \phi_{\pi} + \phi_h \|_{\omega}$$

$$\lesssim h \|\phi_{\pi} + \phi_h\|_{0,\Omega} \| \phi_{\pi} + \phi_h \|_{\omega}.$$

Finally, error estimate (22) follows directly from Theorem 1.

## Model problems and applications

This section presents a series of model problems, building on the framework established earlier. We gradually increase the complexity, beginning with a time-dependent parabolic problem featuring a heterogeneous diffusion. This helps to tackle a biologically motivated optimal control problem involving photobleaching in the endoplasmic reticulum of budding yeast. We then introduce a time-dependent level–set problem, formulated using the weak gradient (1). This serves as a foundation for future work on multiphase flow modeling [42].

## Weak Galerkin method for Helmholtz problem

To address the unsteady heterogeneous diffusion setting, we first introduce a Helmholtz problem, replacing the Laplacian by the Helmholtz operator  $\mathcal{H} = I - \Delta$ , with I the identity operator, to ensure uniqueness.

We seek *u* satisfying

$$\mathcal{H}u = f$$
, in  $\Omega$ , and  $\nabla u \cdot \mathbf{n} = \gamma$ , on  $\partial \Omega$ .

Here,  $f \in H^{-1}(\Omega)$  and  $g \in H^{-1/2}(\Omega)$ . In analogy with (5), the variational formulation reads:

$$a_h^N(u_h, \xi_h) = (f, \xi_h)_{\mathcal{M}_h} + (\gamma, \xi_h)_{\mathcal{E}_h^b},$$

with

$$a_{h}^{N}(u_{h},\xi_{h}) = \left(u_{h},\xi_{h}\right)_{\mathcal{M}_{h}} + \left(\nabla_{\omega}u_{h},\nabla_{\omega}\xi_{h}\right)_{\mathcal{M}_{h}} + \sum_{F\in\mathscr{E}_{h}^{i}} \frac{\eta}{h_{F}^{1/2}} \int_{F} \{\!\!\{\nabla v\}\!\!\} \cdot \mathbf{n}_{F} \, [\!\![\xi_{h}]\!\!] + \sum_{F\in\mathscr{E}_{h}^{i}} \frac{\delta\eta}{h_{F}^{1/2}} \int_{F} [\!\![v]\!\!] \{\!\!\{\nabla \xi_{h}\}\!\!\} \cdot \mathbf{n}_{F}.$$

## Diffusion-dependent problem with heterogeneity

To tackle the yeast problem, we first consider a spatially varying heterogeneous and positive diffusion field  $\omega \in L^{\infty}(\Omega)$ . Given  $f \in L^{2}(\Omega)$ , the continuous problem reads:

*Find*  $u:\Omega \to \mathbb{R}$  *such that* 

$$\partial_t u - \nabla \cdot (\omega \nabla u) = f, \quad \text{in } (0, T) \times \Omega,$$

$$u(0, .) = u_0(.), \quad \text{in } \Omega,$$

$$u = 0, \quad \text{on } (0, T) \times \partial \Omega.$$
(23)

The diffusive flux  $-\omega \nabla u$  lies in  $H(\text{div};\Omega)$ . For the targeted application in Subsection 4,  $\omega$  is required to have discontinuities across subdomains of the endoplasmic reticulum [43]. The problem addressed here (23) will correspond, in a sense, to the direct problem in the yeast test. Superscripts denote time-step indices. Time discretization uses the second-order backward differentiation formula, initialized with  $u^{-1} = u^0$  for convenience. The bilinear form (6) is modified to ensure consistency as follows:

$$a_h^{\boldsymbol{\omega}}(\boldsymbol{v}, \xi_h) \coloneqq \int_{\mathcal{M}_h} \boldsymbol{\omega} \, \boldsymbol{\nabla}_{\boldsymbol{\omega}} \boldsymbol{v} \cdot \boldsymbol{\nabla}_{\boldsymbol{\omega}} \xi_h + \int_{\mathscr{E}_h^i} \frac{\eta}{\sqrt{h_T}} \{\!\!\{ \boldsymbol{\omega} \boldsymbol{\nabla} \boldsymbol{v} \}\!\!\} \cdot \mathbf{n}_F \, [\![\xi_h]\!] + \int_{\mathscr{E}_h^i} \frac{\delta \eta}{\sqrt{h_T}} [\![\boldsymbol{v}]\!] \, \{\!\!\{ \boldsymbol{\omega} \boldsymbol{\nabla} \xi_h \}\!\!\} \cdot \mathbf{n}_F,$$

for every  $v \in W_{\star h}$  and  $\xi_h \in W_h^0$ . For any  $n \ge 1$ , the weak formulation reads:

$$(3u_h^{n+1},\xi_h)_{\mathcal{M}_h} + 2\Delta t \, a_h^{\omega}(u_h^{n+1},\xi_h) = (4u_h^n - u_h^{n-1} + 2\Delta t \, f^{n+1},\xi_h)_{\mathcal{M}_h}, \qquad \forall \xi_h \in W_h.$$

It is worth noting that model (23) captures piecewise-constant diffusivities and jump conditions across internal interfaces (see, e.g., Example 5 and Figure 14), mirroring the mother, bud, and budneck subdomains of the ER. In such settings, the solution remains continuous but not differentiable; this is precisely the setting where the present method can be particularly advantageous, as the interface term acts locally yet preserves consistency on polytopal meshes. The tests presented in the first part of Example 5, therefore, serve as simplified yet representative versions of the ER problem before moving to the full 3D geometry and data-driven parameter identification.

## Optimal control problem with heterogeneous diffusion in yeast cell

We use the aforementioned WG framework to simulate the dynamics of fluorescent molecules within the endoplasmic reticulum (ER) during yeast cell division, using a geometry extracted from experimental imaging and lab data [44]. The ER is partitioned into the mother region  $\Omega_m$ , bud region  $\Omega_b$ , and the sheet-like bud-neck  $\Omega_r$ ; see Figure 16. We formulate a PDE-constrained optimization to infer heterogeneous diffusion within these domains, assuming that diffusion occurs inside the ER volume. FLIP experiments repeatedly bleach a region with intense light, causing fluorescence loss driven by molecular mobility [45]. When applied to  $\Omega_b$ , fluorescence drops rapidly there but decays slowly in  $\Omega_m$ , revealing compartmentalization [43]. This was studied using continuous Galerkin in [44].

We here study heterogeneous volumetric diffusion in the ER, following a photobleaching in the bud. Post-bleach dynamics is simulated using the WG framework. A brief outline of the optimal control formulation is provided. Let u be the concentration at  $t \in (0, T)$ . The control variables  $\omega_m$ ,  $\omega_b$ , and  $\omega_r$  are the diffusion coefficients in  $\Omega_m$ ,  $\Omega_b$ , and  $\Omega_r$ , respectively. The total diffusion function is  $\omega = \omega_m \chi_m + \omega_b \chi_b + \omega_r \chi_r \in L^{\infty}(\Omega)$ , where  $\chi_i$  is the characteristic function of  $\Omega_i$ . A penalty approach is employed [46], with  $1/\varepsilon$  enforcing intensity reduction in a small bleached region  $\Omega_1$ , represented by the characteristic function  $\chi$ . Given  $(u_0, \omega_m, \omega_b, \omega_r)$ , the direct problem

writes

$$\partial_t u - \operatorname{div}(\omega \nabla u) + \frac{1}{\varepsilon} \chi u = 0, \quad \text{in } (0, T) \times \Omega,$$

$$u(0, \cdot) = u_0(\cdot), \quad \text{in } \Omega.$$
(24)

Experimental measurements yield compartment-specific fluorescence loss over (0, T), normalized to pre-bleaching levels. Let  $F_m(t)$  and  $F_b(t)$  denote the averaged fluorescence signals in  $\Omega_m$  and  $\Omega_b$ , respectively, obtained from twenty experiments with bleaching in  $\Omega_1$  (see [44]). The inverse problem seeks the optimal diffusion parameters  $(\omega_m^{\star}, \omega_b^{\star}, \omega_r^{\star})$  that best match the model predictions to the target measured fluorescence functions  $F_l(t)$ , for  $l \in \{m, b\}$ . The problem writes:

$$(\omega_m^{\star}, \omega_b^{\star}, \omega_r^{\star}) = \underset{\omega_j}{\operatorname{arg inf}} E(u; \omega_m, \omega_b, \omega_r),$$

subject to (24) as a constraint. The cost function is:

$$E(u; \omega_m, \omega_b, \omega_r) = \sum_{i \in \{m, b\}} \frac{\alpha_i}{2} \left( \int_{\Omega_{i,T}} u - \int_0^T F_i(t) \int_{\Omega_i} u_0 \right)^2 + \sum_{j \in \{m, b, r\}} \frac{\delta_j}{2} \omega_j^2 + \frac{\delta}{2} |\omega_m - \omega_b|^2.$$

The terms scaled by  $\alpha_l$  measure the mismatch between simulated and observed fluorescence, while the  $\delta$ -term enforces similar diffusion behavior across  $\Omega_m$  and  $\Omega_b$  as biologically expected. The Tikhonov regularization terms  $\delta_j$  mitigate potential ill-posedness and prevent uncontrolled parameter growth.

Let v be the adjoint variable associated with the state u. We define the Lagrangian  $\mathcal{L}$  and derive the optimality conditions. The adjoint equation is obtained by enforcing  $D\mathcal{L}[\delta_u] = 0$ . Given u and control parameters  $\omega_j$ , j = m, b, r, the adjoint problem reads:

$$-\partial_t v - \operatorname{div}(\boldsymbol{\omega} \nabla v) + \frac{1}{\varepsilon} v \chi = \sum_{k=m,b} \alpha_k \left( \int_{\Omega_{k,T}} u - \int_{\Omega_{k,T}} F_k u_0 \right) \chi_k, \tag{25}$$

in  $(0,T) \times \Omega$ . Since adjoint equations evolve backward in time, they require terminal conditions  $v(T,\cdot)=0$  in  $\Omega$ . Rather than explicitly computing the optimal controls at each iteration, a gradient-based optimization algorithm updates the control variables iteratively, driven by the Gâteaux derivative of  $\mathcal L$  in the control variables.

## Time-dependent level-set problem - towards multiphase modeling

To illustrate the weak gradient applicability in multiphysics contexts, we consider its use for steady advection–reaction and time-dependent level–set problems. Multiphase flow simulations [42, 47, 48] pose challenges due to mass loss. In fact, global mass correction [49] can induce non-physical behavior, highlighting the need for approaches with improved mass conservation. Let  $\mu \in L^{\infty}(\Omega)$  and  $\beta$  be a Lipschitz continuous vector. The stationary advection–reaction problem reads:

$$\boldsymbol{\beta} \cdot \boldsymbol{\nabla} \varphi + \mu \varphi = f, \quad \text{in } \Omega, \tag{26}$$

with  $\varphi = \varphi_b$  on the upstream boundary. The  $L^2$ -coercivity requires a uniformly positive  $\mu - \frac{1}{2}\nabla$ .  $\beta > 0$ . The exact solution is assumed in  $W_* := W \cap H^1(\mathcal{M}_h)$ , with W the graph space. The inflow boundary condition is imposed weakly. Set  $\kappa = k$  and  $W_h := \mathbb{P}_d^k(\mathcal{M}_h)$ , the problem reads:

$$a_h^{\boldsymbol{\beta}}(v,\xi_h) = \int_{\Omega} f \xi_h, \quad \forall v \in W_{\star} + W_h, \text{ and } \xi_h \in W_h,$$

with

$$a_h^{\boldsymbol{\beta}}(v,\xi_h) = \sum_{T \in \mathcal{M}_h} \int_T \mu v \xi_h + \boldsymbol{\beta} \cdot \boldsymbol{\nabla} u \xi_h + \sum_{F \in \mathcal{E}_h^i} \int_F \frac{\eta}{h_F^{1/2}} \llbracket v \rrbracket \{\!\!\{\xi_h\}\!\!\} \boldsymbol{\beta} \cdot \mathbf{n}_F + \int_{\partial \Omega} (\boldsymbol{\beta} \cdot \mathbf{n}_F)^{\odot} v \xi_h.$$

Here,  $x^{\odot} = (|x| - x)/2$ . Consistency is verified by substituting u into  $a_h^{\beta}$ , while discrete stability is readily established for  $W_h$ . Rigorous mathematical proofs will be presented in future work. We next turn to the level–set method, which is an interface–capturing approach. Let  $\varphi$  be a level-set function, initially defined as a signed-distance. At each  $t \in (0,T)$ , the deformable interface is represented as

$$\mathcal{I}(t) = \{ \boldsymbol{\xi} \in \Omega \text{ such that } \varphi(t, \boldsymbol{\xi}) = 0 \}.$$

Let  $\beta$  be a prescribed advection vector. With inflow boundary conditions,  $\varphi$  evolves according to the Hamilton–Jacobi equation:

$$\partial_t \varphi + \boldsymbol{\beta} \cdot \boldsymbol{\nabla} \varphi = 0$$
, in  $(0, T) \times \Omega$ .

## **Numerical experiments**

Hereafter, we report computational results validating the theoretical analysis and highlighting the accuracy of the weak Galerkin approach. Simulations are carried out on the Almesbar HPC cluster (204 CPU nodes), employing up to 52 cores for 3D cases. Each node hosts dual Intel Xeon Gold 6230R CPUs (Cascade Lake, 26 cores, 2.1GHz, Q1 2020).

The framework is implemented within the C++ library Rheolef [50]. Parallel computations use MPI<sup>1</sup>, with MUMPS handling matrix factorization and direct solves on distributed-memory systems. Meshes are generated via Gmsh [51]. The post-processing is done with Paraview<sup>2</sup> and Gnuplot<sup>3</sup>.

## Example 1: Two-dimensional validation: convergence analysis

Consider a known exact solution to assess convergence. For  $\mathbf{x} = (x, y) \in \Omega = [0, 1.5]^2$ , define

$$u(\mathbf{x}) = xy(1-x)(1-y)e^{x-y}$$
.

<sup>1</sup> http://www.mpich.org, version 4.3.0, 2025-05-30.

<sup>2</sup> https://www.paraview.org, version 5.13, 2025-05-30.

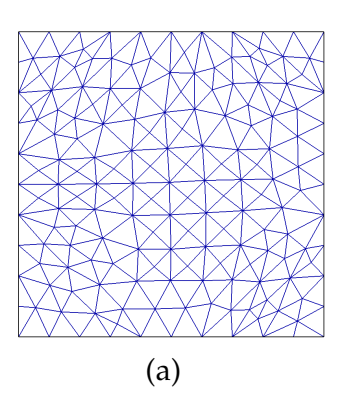
<sup>3</sup> http://www.gnuplot.info, version 6.0.1, 2025-05-30.

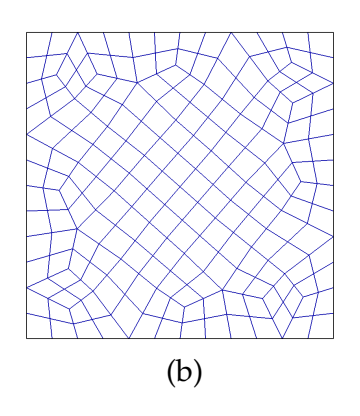
Aymen Laadhari

**Table 1.** 2D Test case. Error and convergence rates under mesh refinement for different parameter sets (k, κ, δ, N<sub>∂T</sub>), using low-order polynomial approximations ROC ROC 1.97 2.00 2.90 2.97 2.97 2.98 2.98 1.91 2.01 2.01 (2, 4, 0.5, 3)(1,1,0,3)1.820E-3 1.237E-4 3.097E-5 7.702E-6 .913E-6  $\|\epsilon_h\|_{0,\Omega}$ 5.903E-6 7.489E-7 9.490E-8 1.207E-8 1.857E-4 4.640E-5 3.631E-4 $\|\epsilon_h\|_{0,\Omega}$ 6.052E-3 ROC ROC 1.30 1.89 1.95 1.97 1.99 2.88 2.96 2.97 2.98 2.99 2.99 1.73 (2, 4, 1, 3)(1,1,1,3)1.853E-6 1.183E-8 2.922E-5 7.374E-6 7.483E-7  $\|\epsilon_h\|_{0,\Omega}$ 3.626E-4 4.651E-5 5.916E-6 9.424E-8 ..642E-3 4.431E-4 1.148E-4  $\|e_h\|_{0,\Omega}$ 5.460E-3 ROC ROC 1.96 2.00 2.72 2.86 2.94 2.96 1.49 2.01 2.01 2.91 1.84 2.01 (1,3,-1,3)(2, 2, 1, 3)1.248E-4 7.680E-6 3.098E-5 9.215E-8 1.906E-6 4.143E-5 5.520E-6 7.190E-7 1.169E-8 1.940E-3 1.990E-4 3.005E-4  $|\epsilon_h|_{0,\Omega}$ 6.935E-3  $\epsilon_h \|_{0,\Omega}$ 1.95 2.02 2.02 ROC 2.65 3.10 2.88 2.00 3.01 1.40 2.31 (1,2,-1,3)(2, 4, 0, 3)3.182E-5 7.843E-6  $\|\epsilon_h\|_{0,\Omega}$ 3.818E-6 1.995E-3 5.169E-4 1.290E-4 .936E-6 2.057E-4 3.275E-5 5.195E-7 6.439E-8 8.132E-9 6.915E-3  $\|\epsilon_h\|_{0,\Omega}$ ROC ROC 2.85 1.76 1.94 2.00 2.03 2.03 2.17 2.59 3.04 2.98 1.31 (1, 1, -1, 3)for  $u_h$  on triangular meshes (2, 2, 0, 3)6.961E-3 2.059E-3 3.292E-5 8.058E-6  $\|\epsilon_h\|_{0,\Omega}$ 3.002E-5 3.647E-6 6.401E-8 5.382E-4 1.808E-4 5.066E-7 8.183E-9  $\|\epsilon_h\|_{0,\Omega}$ 1.341E-4 .977E-6 128 256 16 32 16 32 64 64

polynomial approximations **Table 2.** 2D Test case. Spatial convergence in both norms under mesh refinement for parameter sets  $(k, \kappa)$  with  $\delta = 0$  and  $N_{\partial T} = 3$ , computed with higher-order

$ \begin{array}{c c c c c c c c c c c c c c c c c c c $	128 9.811E-10 3.00	64 7.854E-9 3.00	32 6.301E-8 3.02	16 5.099E-7 3.07	8 4.277E-6 3.25	4 4.080E-5 3.68	$1/h$ $\ \varepsilon_h\ _{\omega}$ ROC	64 6.292E-11 4.03	32 1.029E-9 4.05	16 1.706E-8 4.06	8 2.853E-7 4.05	4 4.740E-6 3.96	$1/h$ $\ \epsilon_h\ _{0,\Omega}$ ROC	$(k, \kappa) = \tag{3,3}$	polynomial approximations	Hall a 2D Host area Constitution	128 1.634E-8 3.00	64 1.311E-7 3.01	32 1.054E-6 3.01	16 8.499E-6 3.02	8 6.892E-5 3.04	4 5.680E-4 3.10	$1/h$ $\ \epsilon_h\ _{\omega}$ ROC	64 2.723E-10 3.99	32 4.328E-9 3.99	16 6.863E-8 3.98	8 1.085E-6 3.97	4 1.703E-5 3.90	$1/h$ $\ e_h\ _{0,\Omega}$ ROC	$(k,\kappa) = (3,3)$
ROC $\ e_h\ _{0,\Omega}$ $ e_h _{0$														(3,6)	Serice ni poni norme and															(3,5)
$4,4$ ) $(5,5)$ ROC $\ \epsilon_h\ _{0,\Omega}$ ROC $\ \epsilon_h\ _{0,\Omega}$ $4.92$ $7.475E.9$ $6.10$ $1.06$ $4.96$ $1.112E-10$ $6.07$ $8.28$ $0$ $4.97$ $1.690E-12$ $6.04$ $$ $1$ $4.95$ $$ $$ $$ $1$ $4.95$ $$ $$ $$ $1$ $4.95$ $$ $$ $$ $1$ $4.18$ $5.081E-7$ $5.17$ $1.31$ $4$ $4.12$ $1.548E-8$ $5.04$ $1.98$ $4$ $4.09$ $4.839E-10$ $5.00$ $3.06$ $4$ $4.07$ $1.515E-11$ $5.00$ $3.06$ $4$ $4.07$ $1.515E-11$ $5.00$ $$	3.00							4.00						(4	и пезнаетненная р		3.00							4.00						
		3.99	4.00	3.99	3.96	3.87	ROC		4.94	4.90	4.90	4.84	ROC	<b>i</b> ,7)	arameter sets (n, n)								ROC		,				ROC	(4,4)
ROC $\  \epsilon_l \ $ 6.10       1.06         6.07       8.28         6.04       -          -         5.07       1.31         5.00       3.06         5.00       -          -          -         5.88       1.22         5.97       9.91         5.99       -          -         4.92       1.34         4.98       2.13         4.99       5.26          -          -          -          -          -          -          -          -          -          -          -          -          -          -          -          -          -          -          - <t< td=""><td></td><td> </td><td> </td><td>6.22436e-11</td><td>1.98227e-09</td><td>6.23815e-08</td><td><math>\ e_h\ _{\omega}</math></td><td> </td><td> </td><td>2.76107e-13</td><td>1.76087e-11</td><td>1.10024e-09</td><td><math>\ \epsilon_h\ _{0,\Omega}</math></td><td>(5,8)</td><th><math>\frac{1}{2}</math> with <math>\frac{1}{2}</math></th><td>14 F == 0 3 41:</td><td> </td><td> </td><td>1.515E-11</td><td>4.839E-10</td><td>1.548E-8</td><td>5.081E-7</td><td><math display="block">\ e_h\ _{\omega}</math></td><td>-</td><td></td><td>1.690E-12</td><td>1.112E-10</td><td>7.475E-9</td><td><math>\ \epsilon_h\ _{0,\Omega}</math></td><td>(5,5)</td></t<>				6.22436e-11	1.98227e-09	6.23815e-08	$\ e_h\ _{\omega}$			2.76107e-13	1.76087e-11	1.10024e-09	$\ \epsilon_h\ _{0,\Omega}$	(5,8)	$\frac{1}{2}$ with $\frac{1}{2}$	14 F == 0 3 41:			1.515E-11	4.839E-10	1.548E-8	5.081E-7	$\ e_h\ _{\omega}$	-		1.690E-12	1.112E-10	7.475E-9	$\ \epsilon_h\ _{0,\Omega}$	(5,5)
				4.99 5.261E-13	4.98 2.134E-11	4.92 1.343E-9	ROC $\ \epsilon_h\ _{\omega}$			5.99 -	5.97 9.917E-14	5.88 1.229E-11	ROC $\ \epsilon_h\ _{0,\Omega}$		$g_T=4$ , computed	1 2222222			5.00 –	5.00 3.064E-12	5.04 1.985E-10	5.17 1.311E-8	ROC $\ e_h\ _{\omega}$			6.04 -	6.07 8.282E-13	6.10 1.067E-10	ROC $\ \epsilon_h\ _{0,\Omega}$	





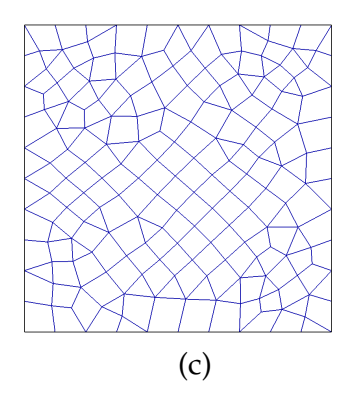


**Figure 1.** Examples of 2D meshes with different element types composed of: (a) triangles  $(N_{\partial T}=3)$ , (b) quadrilateral elements  $(N_{\partial T}=4)$ , (c) both triangles and quadrilaterals  $(N_{\partial T}=4)$ 

Accordingly, *f* can be expressed explicitly as:

$$f(\mathbf{x}) = -2x(y-1)(y-2x+xy+2)e^{x-y}.$$

Let  $\epsilon_h := u - u_h$  be the discretization error. Unstructured quasi-uniform meshes are generated using different element types: triangles ( $N_{\partial T} = 3$ ) and quadrangles ( $N_{\partial T} = 4$ ), as shown in Figure 1.

Spatial accuracy is assessed by computing the  $\|\cdot\|_{\omega}$ - and  $L^2$ -errors over a sequence of mesh refinements. The rate of convergence, denoted by ROC, between refinement levels r-1 and r is

$$ROC = \frac{\log(E_{r-1}/E_r)}{\log(h_{r-1}/h_r)}, \quad r \ge 1,$$

with  $E_r \in \{\|\epsilon_h^{(r)}\|_{0,\Omega}, \|\|\epsilon_h^{(r)}\|\|_{\omega}\}$  the error at level r in the chosen norm, and  $h_r$  the characteristic mesh size at level r.

Various approximation spaces are considered for  $u_h$  and the weak gradient. Initially,  $\delta = -1$  is set, and  $\mathbb{P}_1$  approximations are used for  $u_h$ . By varying the degree of polynomial approximation for the weak gradient discretization,  $L^2$ -error convergence is reported. The results in Table 1 align with the theory: for k = 1, Theorem 2 predicts  $\|\epsilon_h\|_{0,\Omega} = \mathcal{O}(h^{k+1}) = \mathcal{O}(h^2)$ , and the observed ROC approaches 2 across all  $(\kappa, \delta)$  choices. Varying  $\kappa$  at fixed k mainly affects pre-asymptotic constants on coarse meshes.

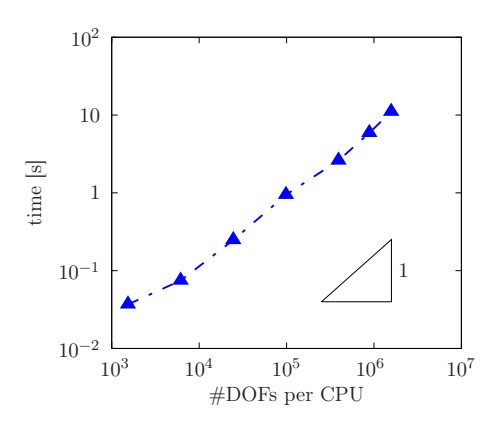
We then vary  $\delta \in \{-1,0,1\}$ . Optimal convergence is observed for  $\delta = 1$  (i.e. when  $a_h$  is symmetric) and likewise for  $\delta \in \{0,-1\}$ . The polynomial approximation degree is then increased by setting k=2. In this setting as well, the choices  $\delta \in \{0,0.5,1\}$  leave the asymptotic order unchanged. In addition, the computations attain the expected  $L^2$  accuracy order on triangular meshes, even when  $\kappa$  is smaller than  $k+N_{\partial T}-1$ , for various values of  $\delta$ . In what follows, we set  $\delta=0$ , unless otherwise mentioned.

Consider now higher-order polynomial degrees with  $k \geqslant 3$  on triangular mesh sequences. Table 2 demonstrates optimal convergence that aligns with the theoretical rates in both the  $L^2$  and  $\|\cdot\|_{\omega}$  norms. Note that, at finer mesh resolutions, round-off errors eventually influence the convergence order once the error reaches a threshold value.

For k = 3, 4, 5, 6, the measured ROCs in  $L^2$  are close to k + 1 and those in  $\|\cdot\|_{\omega}$  are close to k, exactly as predicted by Theorem 1 and Theorem 2. The slight departures on the finest levels (where the errors reach  $\sim 10^{-11}$ – $10^{-13}$ ) are consistent with round-off effects rather than a loss of asymptotic

Unstructured triangular meshes are used **Table 4.** Example 1. Spatial convergence in 2D for the Laplace–Dirichlet problem for various values of the stabilization parameter  $\eta$  with fixed  $k = \kappa = 3$  and  $\delta = 1$ .

8	$\ \epsilon_h\ _{0,\Omega}$ 1.839E-5 1.136E-6	ROC 4.01 4.02	$\ \epsilon_h\ _{0,\Omega}$ $1.667E-5$ $1.073E-6$	ROC 3.89 3.96	3.7	$\ \epsilon_h\ _{0,\Omega}$ $\ \epsilon_h\ _{0,\Omega}$ 4.468E-5 3.741E-5	ROC 3.94 0.26	$\ \epsilon_{l}$ 7.93	J. J.	0.2	0.2 ROC 4.75 2.70
1.136E-6 7.057E-8		4.02 4.01	1.073E-6 6.824E-8	3.96 3.98	ω ω 21 21	3.741E-5 3.725E-7		0.26 6.65			1.223E-5 2.468E-5
4.401E-9		4.00	4.315E-9	3.98	3.2	3.239E-9		6.85	6.85 3.519E-5	3.519E-5	3.519E-5 -0.51
2.749E-10	-10 -11	4.00 3.98	2.718E-10 1.731E-11	3.99 3.97	2.1: 1.4:	2.121E-10 1.430E-11		3.93 3.89		1.235E-9 1.679F-11	1.235E-9 14.80 1.679F-11 6.20
<u>e</u>	$\ \epsilon_h\ _{\omega}$	ROC	$\ e_h\ _\omega$	ROC		$\ \epsilon_h\ _{\omega}$		ROC		$\ e_h\ _{\omega}$	$\ e_h\ _{\omega}$ ROC
5.2	5.216E-4	2.96	5.876E-4	3.04	1.7	1.719E-3		2.99	<b>(.)</b>	3.108E-3	3.108E-3 3.60
6.6	6.663E-5	2.97	7.225E-5	3.02	2.6	2.692E-3		-0.65		9.415E-4	9.415E-4 1.72
8.	8.423E-6	2.98	8.906E-6	3.02	5.1	5.173E-5		5.70	5.70 3.672E-3	3.672E-3	3.672E-3 -1.96
<u> </u>	L.056E-6	3.00	1.098E-6	3.02	1.4	L.485E-6		5.12			9.891E-3
$\vdash$	1.320E-7	3.00	1.355E-7	3.02	1.7	L.756E-7		3.08		7.241E-7	7.241E-7
<u></u>	.646E-8	3.00	1.676E-8	3.02	2.0	2.097E-8		3.07	3.07 2.931E-8	2.931E-8	2.931E-8



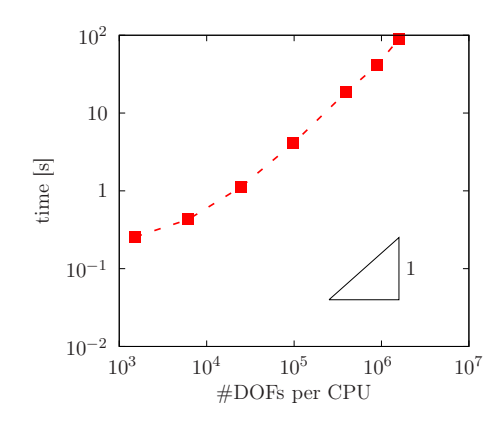


**Figure 2.** Parallel performance: CPU time for (left) assembly and (right) linear solve versus DOFs per processor (log–log scale)

#### behavior.

Next, we examine more general unstructured but quasi-uniform meshes with  $N_{\partial T}=4$ . Convergence in  $L^2$  and  $\|\cdot\|_{\omega}$  norms is studied. Table 3 shows the same trend on polytopal meshes with  $N_{\partial T}=4$ : errors decrease as predicted:  $|\epsilon_h|_{0,\Omega} \sim h^{k+1}$  and  $\|\epsilon_h\|_{\omega} \sim h^k$ . Using  $\kappa=k+N_{\partial T}-1$  (analysis choice) or  $\kappa=k$  (reduced choice for k=3) delivers numerically the same asymptotic rates, indicating that optimal convergence is robust to the choice of element shapes and to the degree used for the weak-gradient unknowns.

Having verified that the measured rates match the theoretical predictions for a range of  $(k,\kappa)$  and mesh types, we next examine the sensitivity to the stabilization parameter  $\eta$ . With fixed approximation spaces, we take  $k=\kappa=3$  for  $u_h$  and the weak gradient and use  $\delta=1$  (symmetric discrete bilinear form) on unstructured triangular meshes. To properly choose  $\eta$  and assess its role, we vary  $\eta\in\{2,1,0.1,0.02,0\}$  and compare against the exact solution in the  $\|\cdot\|_{0,\Omega}$  and  $\|\cdot\|_{\omega}$  norms. Results are presented in Table 4. For  $\eta=2,1,0.1$  the scheme exhibits the predicted optimal rates— $\mathcal{O}(h^4)$  in  $L^2$  and  $\mathcal{O}(h^3)$  in  $\|\cdot\|_{\omega}$ . In contrast, for  $\eta=0.02$  and  $\eta=0$  (no stabilisation), optimality is lost:  $L^2$  and  $\|\cdot\|_{\omega}$  errors stagnate or degrade on fine meshes. This is consistent with the condition in Lemma 3, which requires  $\eta\gtrsim h^{1/2}$ ; with a fixed very small  $\eta$ , the condition is violated as  $h\to 0$ . In the remainder, we set  $\eta=1$  unless stated otherwise.

Thereafter, we briefly assess the runtime and parallel efficiency of our implementation; a thorough performance assessment is not undertaken in this work. We set  $k = \kappa = 2$ ,  $\eta = 10$ , and  $\delta = 1$  on triangular meshes. We focus on the assembly and linear solve steps, which are the most time-consuming.

Figure 2 reports CPU times (on a log–log scale) versus degrees of freedom (DOFs) per processor for both steps. We interpret these plots in terms of *strong scaling*: With the problem size unchanged, ideal behavior halves the runtime when the number of processors doubles (i.e., unit slope when time is plotted against DOFs per processor on a log–log scale). The results show near-ideal strong scaling for finer meshes in both assembly and linear solve, with a degradation on coarser meshes due to reduced work per core and communication overhead. Note that a more systematic scaling study on larger, multiphysics problems will be reported in a forthcoming work based on an extension of the present method.

#### Example 2: Three-dimensional validation: convergence analysis

We now assess errors in the three-dimensional case with  $\Omega = [0, 1]^3$ . A unit cubic geometry is meshed using unstructured quasi-uniform tetrahedral ( $N_{\partial T} = 4$ ) meshes and structured prismatic ( $N_{\partial T} = 5$ ) meshes, as shown in Figure 3. Spatial accuracy is assessed by comparing numerical and

exact solutions after mesh refinements, using errors in  $\|\cdot\|_{\omega}$ ,  $L^2$ ,  $L^{\infty}$ , and  $H^1$  norms. Consider the test case with the exact analytical solution:

$$u(\mathbf{x}) = \sin(2\pi x)\sin(2\pi y)\sin(2\pi z),$$
 in  $\Omega$ .

This corresponds to  $f(\mathbf{x}) = 12\pi^2 u(\mathbf{x})$ .

For polynomial degree approximation k, we set  $\kappa = k$  and  $\delta = 1$ . The error histories presented in Figure 4 confirm optimal convergence rates in the  $\|\cdot\|_{\omega}$  and  $L^2$  norms for tetrahedral meshes. Additionally, the error histories in Figure 5 show convergence rates of order  $h^k$  in the  $H^1$  seminorm and  $h^{k+1}$  in the  $L^{\infty}$  norm.

Thereafter, we consider structured prismatic meshes. The convergence shown in Figure 6 confirms the optimal decay in  $\|\cdot\|_{\omega}$  and  $L^2$  norm as predicted by the theory. Furthermore, the same convergence rates of order  $h^k$  in the  $H^1$  seminorm and  $h^{k+1}$  in the  $L^{\infty}$  norm are observed, consistent with the results for tetrahedral meshes, as illustrated in Figure 7.

We conclude this example with a remark on the symmetry term in the bilinear form (6). Setting  $\delta=1$  renders the discrete bilinear form symmetric (in line with the continuous setting) and this choice is used to prove the  $\|\cdot\|_{0,\Omega}$ -error estimate via an Aubin–Nitsche duality argument; see Theorem 2. In practice, however, we observe the same optimal convergence for several values of  $\delta$ , as highlighted in Example 1. Consider here the 3D test with 196'608 degrees of freedom (take  $\eta=0.75$  and  $N_{\partial T}=4$ ). On 6 cores, the wall-clock time for both assembly and linear solve is 24.4 s

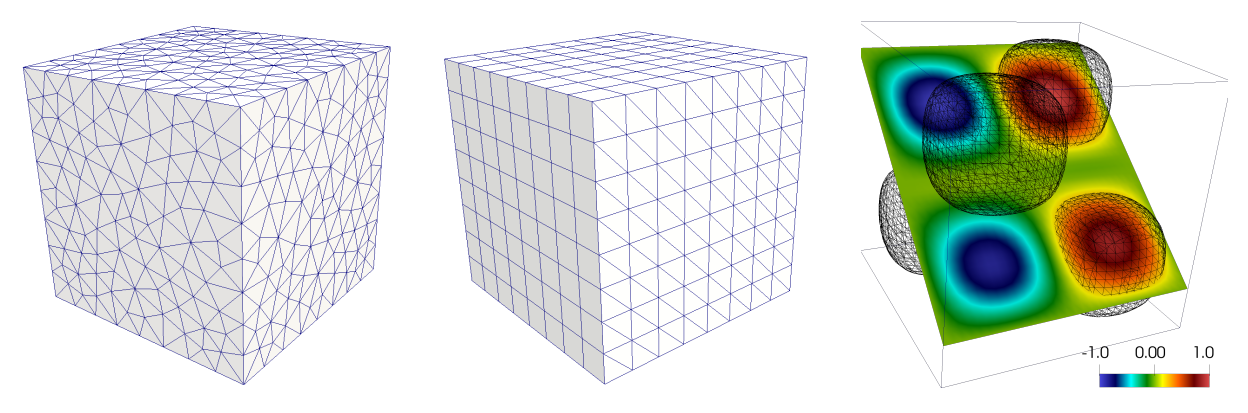


**Figure 3.** Example 2 (3D). (left) tetrahedral meshes. (middle) prismatic meshes. (right) Snapshots showing iso-value 0.5 for  $k=\kappa=2$ ,  $\delta=0.37$ ,  $\eta=0.75$  and  $N_{\partial T}=4$ . HPC computations used 24 computing cores

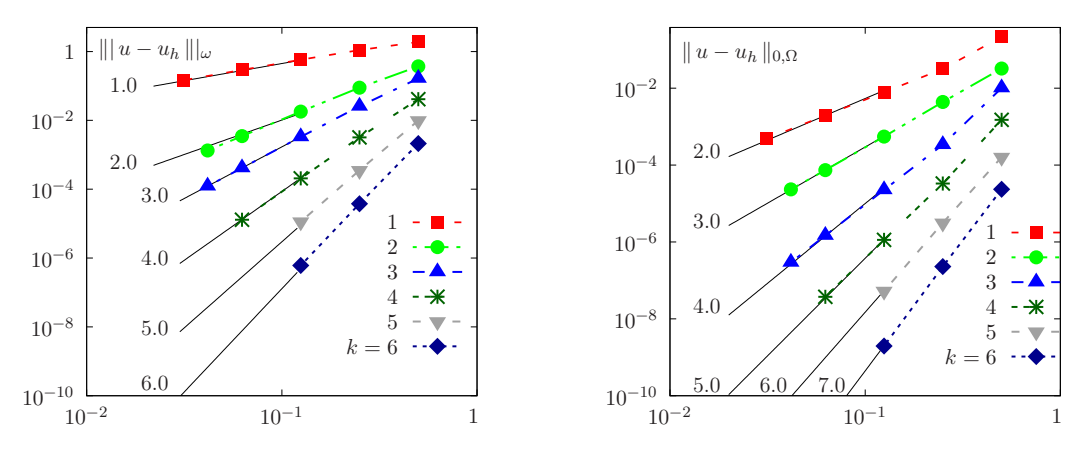


**Figure 4.** Example 2 (3D). Error convergence versus h (log-log scale) for tetrahedral meshes. Solid black lines indicate the theoretical rates

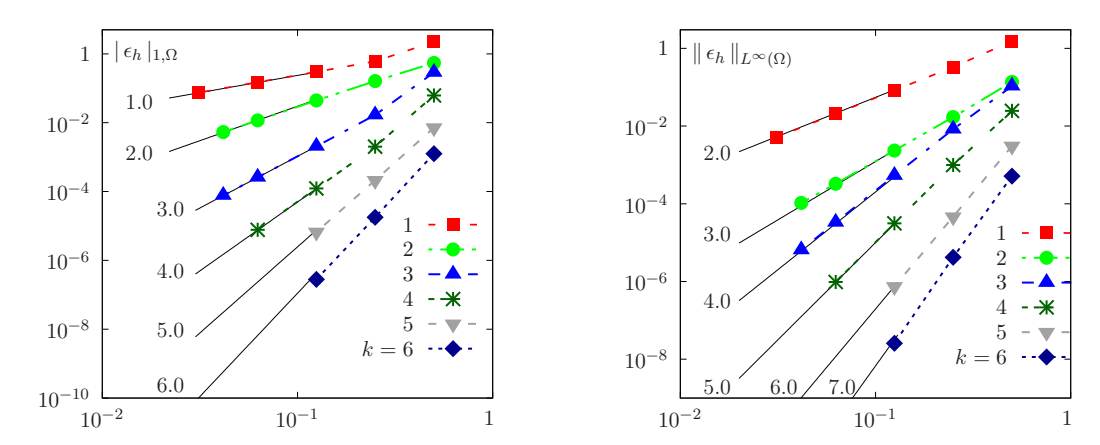


**Figure 5.** Example 2 (3D). Error convergence versus h (log-log scale) for tetrahedral meshes. Solid black lines indicate the theoretical rates

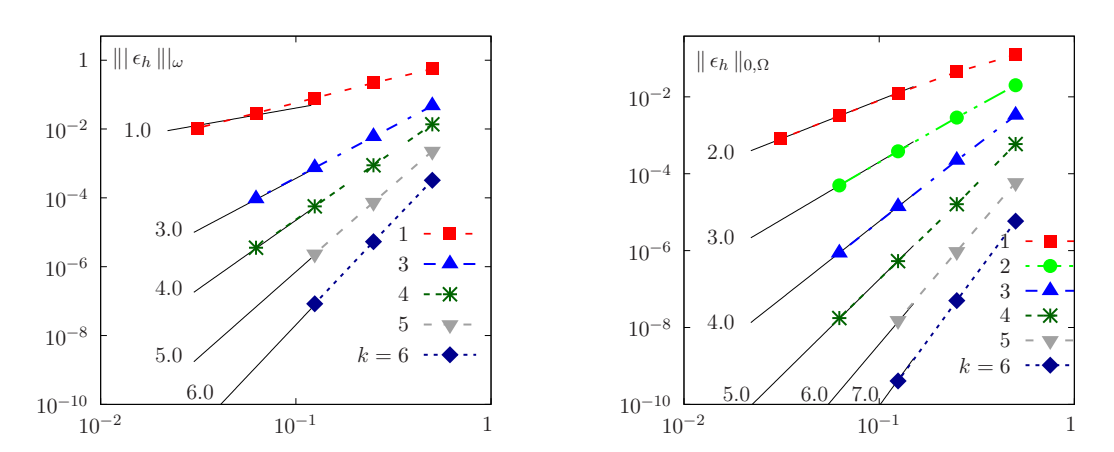


**Figure 6.** Example 2 (3D). Error convergence versus h (log-log scale) for prismatic meshes. Solid black lines indicate the theoretical rates

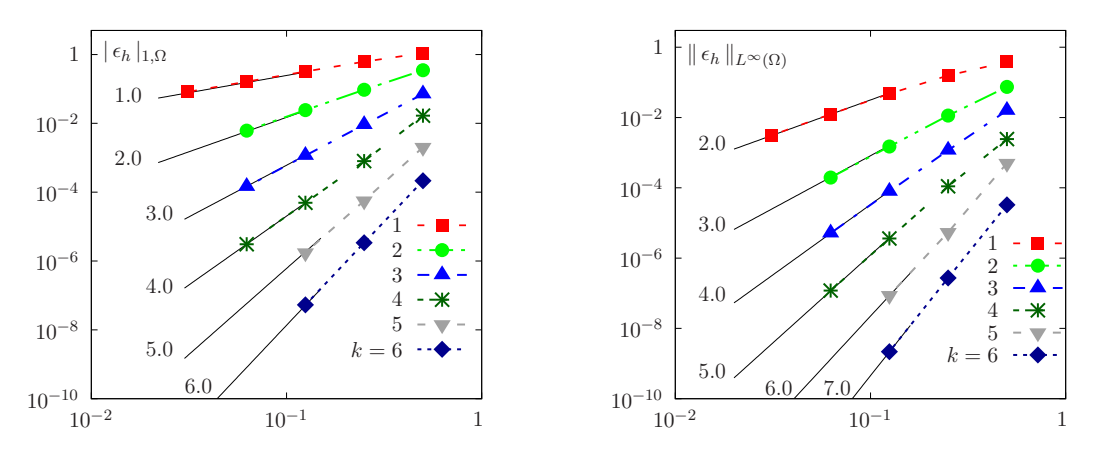


**Figure 7.** Example 2 (3D). Error convergence plotted against h on a log-log scale for prismatic meshes. Solid black lines indicate the theoretical rates

for  $\delta = 1$  versus 24.1 s without assembling the term involving  $\delta$ , indicating also a negligible cost difference in the three-dimensional case.

## **Example 3: Error analysis with curved boundaries**

Herein, we assess the accuracy of domains with non-simplicial boundaries. We consider the unit disk  $\Omega \subset \mathbb{R}^2$  with curved boundary, and generate successively refined unstructured meshes. To

accurately capture the curvature, we use high-degree polynomial approximations for the boundary elements. Figure 8 illustrates sample meshes with high-order boundary edge approximations. For validation, consider a test case with

$$u(\mathbf{x}) = \cos\left(\frac{5\pi}{2} \|\mathbf{x}\|_{2}\right), \text{ with } \|\mathbf{x}\|_{2} = \sqrt{x^{2} + y^{2}}.$$

That corresponds to

$$f(\mathbf{x}) = \begin{cases} \frac{25\pi^2}{4} \left( \frac{2\sin(\frac{5\pi}{2}\|\mathbf{x}\|_2)}{5\pi \|\mathbf{x}\|_2} + \cos(\frac{5\pi}{2}\|\mathbf{x}\|_2) \right), & \text{if } \|\mathbf{x}\|_2 \neq 0, \\ \frac{50\pi^2}{4}, & \text{if } \|\mathbf{x}\|_2 = 0. \end{cases}$$

The error history and convergence rates are presented in Figure 9 for several  $k \in \{1, 2, 3, 4\}$ , with  $\kappa = k + N_{\partial T} - 1$  and a curved boundary depending on the different values of k. Numerical results confirm an optimal convergence, as predicted by the theory.

## Example 4: Helmholtz problem

We now focus on the Helmholtz problem presented in Subsection 4. Accuracy is examined in one, two, and three-dimensional settings.

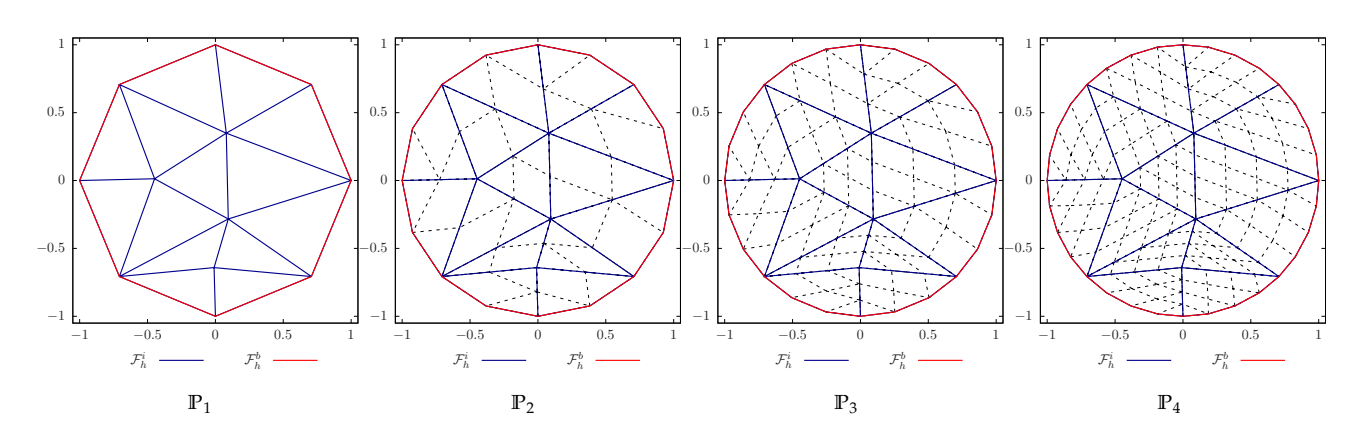
In one dimension (d = 1), consider an analytical solution  $u(x) = \sin(\pi x)$  in a unit domain [0, 1]. The corresponding data are:

$$f(x) = (1 + \pi^2) u(x),$$
  
$$\gamma(x) = -\pi.$$

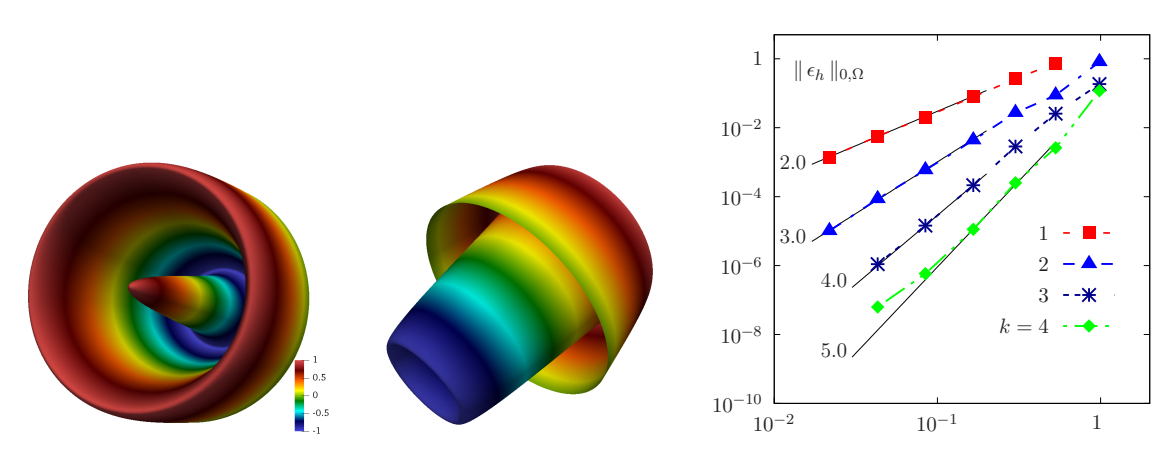
For polynomial degrees k with  $\kappa = k+1$  and  $\delta = 1$ , Figure 10 reports the 1D errors and observed convergence rates in the  $L^2$  and  $\|\cdot\|_{\omega}$  norms. The results confirm the predicted optimal  $L^2$ -error rates of k+1 and  $\|\cdot\|_{\omega}$ -error rates of k, which is consistent with the theoretical analyses.

For d = 2, we take a computational domain  $[0, 1]^2$  and set

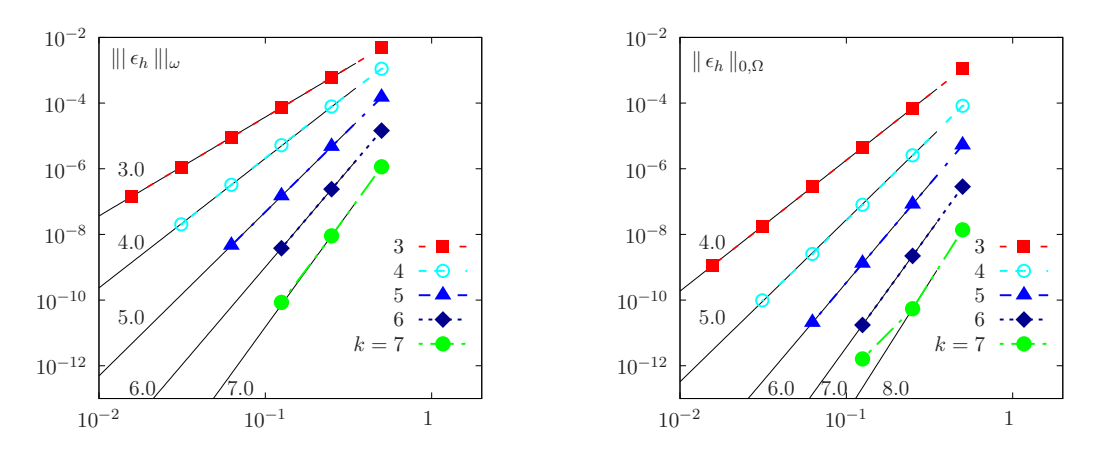
$$u(\mathbf{x}) = \sin(\pi x)\sin(\pi y),$$
  
$$f(\mathbf{x}) = (1 + 2\pi^2)u(\mathbf{x}),$$



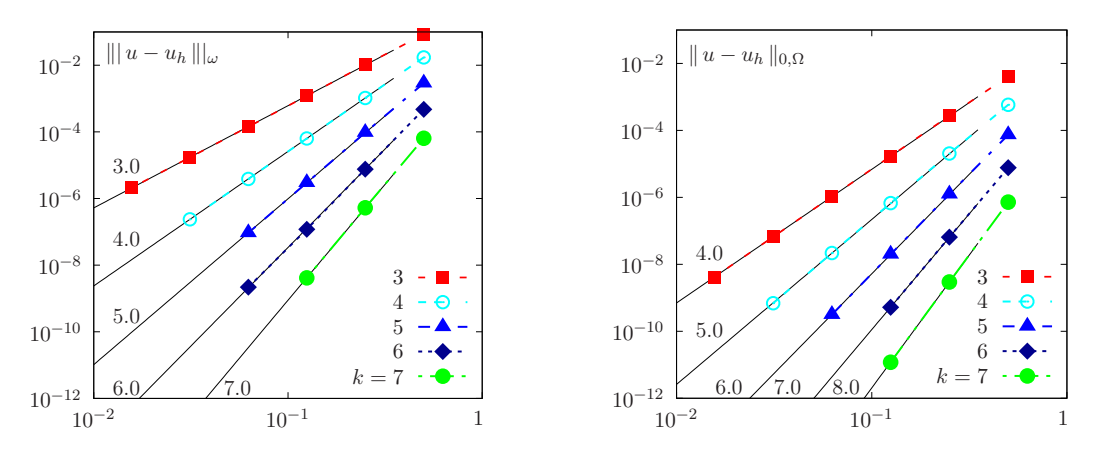
**Figure 8.** Example 3. Unstructured meshes of 14 elements with high-order approximations of the curved boundary



**Figure 9.** Example 3. (left - middle) Solution snapshots computed on  $\mathcal{M}_h$  with  $h_{min}=0.00293133$ ,  $h_{max}=0.0217692$  and  $\delta=1$ . (right) Error convergence computed in the norm  $\|\cdot\|_{0,\Omega}$ . Solid black lines indicate the theoretical rates



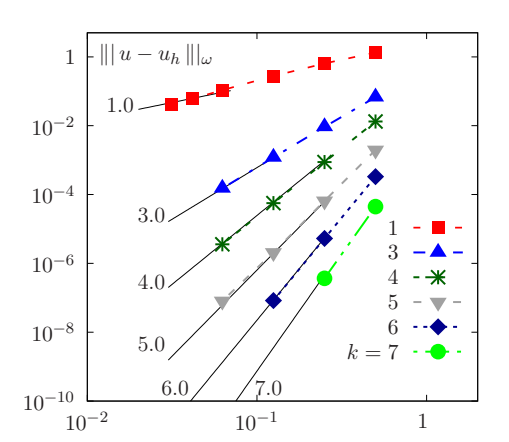
**Figure 10.** Example 4. Spatial convergence in the norms  $\|.\|_{\omega}$  and  $L^2$  plotted with respect to h on a log-log scale for the Helmholtz problem in 1D. Solid black lines indicate the theoretical rates

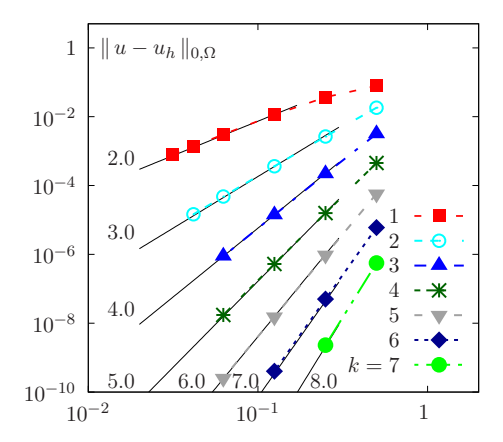


**Figure 11.** Example 4. Spatial error convergence in the norms  $\|.\|_{\omega}$  and  $L^2$  plotted with respect to h on a log-log scale for the Helmholtz problem in 2D. Solid black lines indicate the theoretical rates

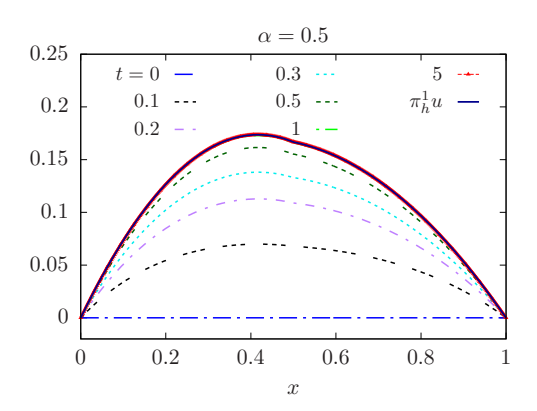
$$\gamma(\mathbf{x}) = -\pi(\sin(\pi x) + \sin(\pi y)).$$

The error history and convergence rates are reported in Figure 11, depicting an optimal convergence in both the  $\|\cdot\|_{\omega}$  and  $L^2$  norms.





**Figure 12.** Example 4. Spatial convergence in the norms  $\|.\|_{\omega}$  and  $L^2$  plotted with respect to h on a log-log scale for the Helmholtz problem in 3D. Tetrahedral meshes are used. Solid black lines indicate the theoretical rates



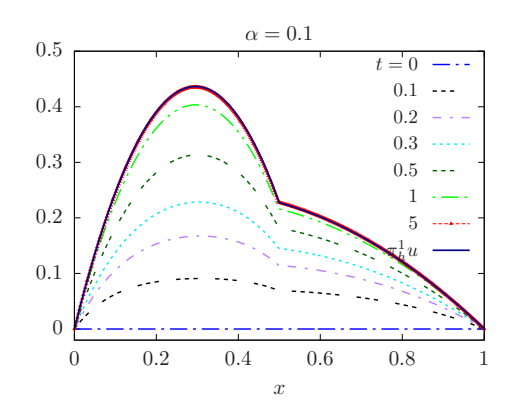


**Figure 13.** Temporal convergence toward the exact solution for heterogeneous diffusion with  $\alpha = 0.5$  (left) and  $\alpha = 0.1$  (right). Computations are performed with h = 1/32 and  $\Delta t = 10^{-1}$ 

In 3D, we consider the unit cube domain together with the following exact analytical solution:

$$u(\mathbf{x}) = \sin(\pi x)\sin(\pi y)\sin(\pi z).$$

The corresponding source and boundary data are:

$$f(\mathbf{x}) = (1 + 3\pi^2)u(\mathbf{x}),$$
  

$$\gamma(\mathbf{x}) = -\pi(\sin(\pi x)\sin(\pi y) + \sin(\pi y)\sin(\pi z) + \sin(\pi z)\sin(\pi x)).$$

Figure 12 confirms optimal convergence in line with theoretical estimates. As errors decrease, the growing system size leads to memory limitations, making direct solvers impractical. Iterative solvers then become necessary and offer a more memory-efficient alternative.

## Example 5: Time-dependent heterogeneous protein diffusion in budding yeast cell

In the first part, we consider the heterogeneous diffusion case described in Subsection 4, with a discontinuous coefficient, piecewise defined as  $\omega(x) = 1$  for  $x \in [0,0.5)$  and  $\omega(x) = \alpha > 0$  for  $x \in [0.5,1]$ . Set f=1 as a constant source term. This one-dimensional study assesses whether the method reproduces the expected  $C^0$ -but not  $C^1$ -steady-state profile under mesh refinement (jump in the derivative). The parameter  $\alpha$  plays the role of a compartment-dependent diffusivity and anticipates the contrast between the mother/bud regions and the bud neck observed in the ER.

This problem thus serves as a simplified surrogate, mirroring the mother/bud/bud-neck partition of the ER while using the same discretization and stabilization choices.

The jump in  $\omega$  across x = 0.5 induces a discontinuity in  $\mathbf{n} \cdot \nabla u$ . The exact steady-state solution of (23) remains continuous but is not differentiable at x = 0.5, as follows:

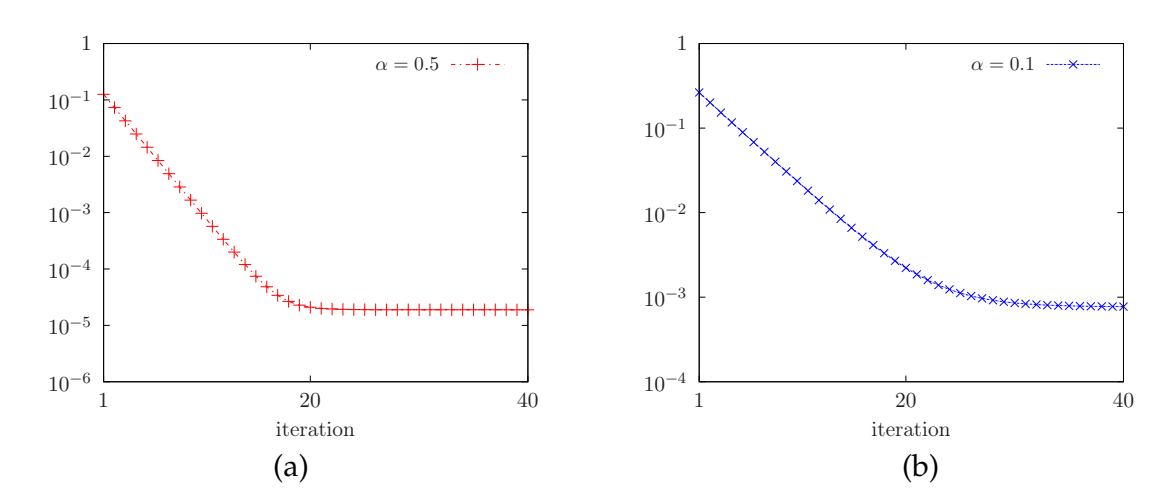
$$u(x) = \begin{cases} \frac{x}{4\alpha} \left( \frac{1+3\alpha}{2(1+\alpha)} - x \right), & \text{in } [0,0.5), \\ \frac{1-x}{2} \left( x + \frac{1-\alpha}{2(1+\alpha)} \right), & \text{otherwise.} \end{cases}$$

Figure 13 illustrates the exact solution for  $\alpha = 0.5$  and  $\alpha = 0.1$ . As expected, the discontinuity in the derivative at x = 0.5 becomes more pronounced as diffusion heterogeneity increases.

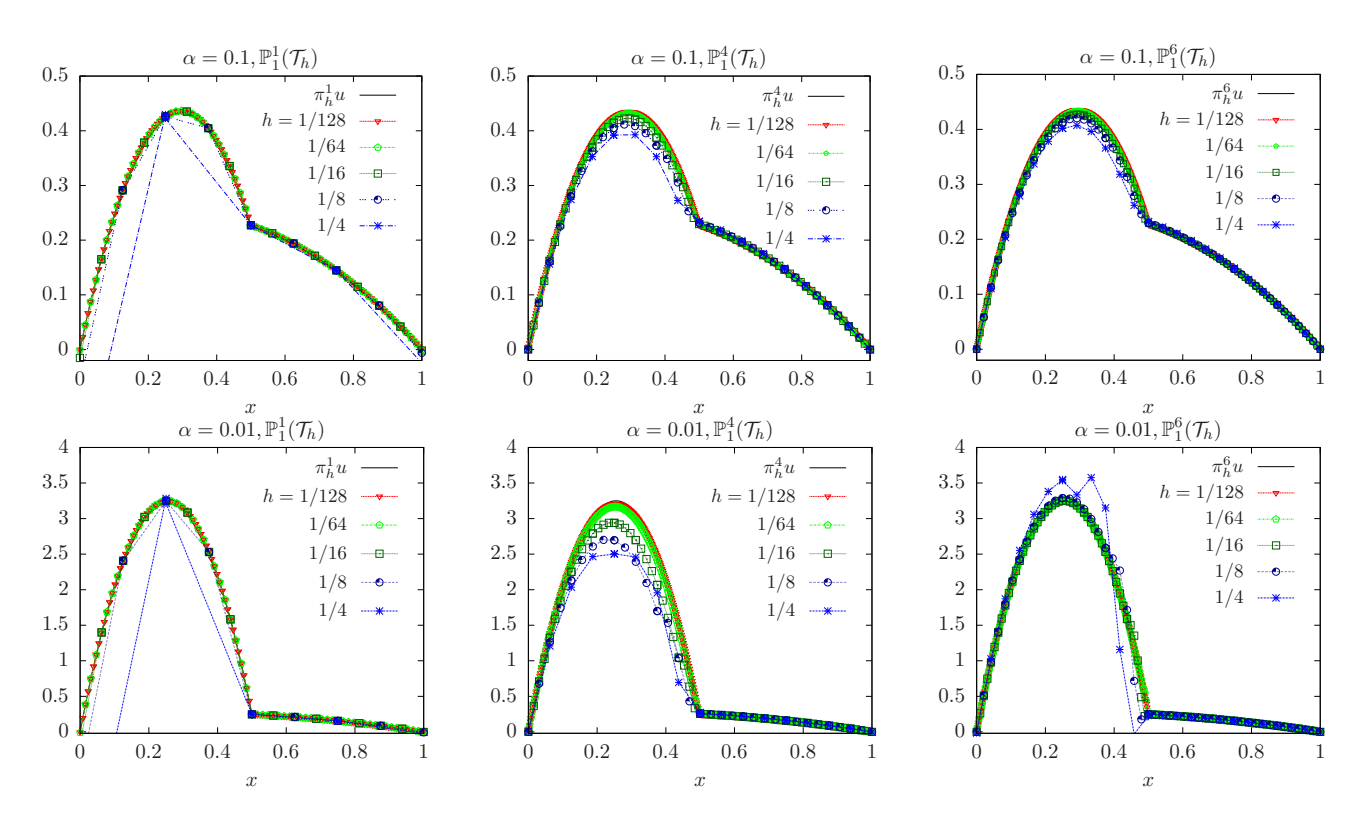
To complement the analytical consistency proof, we have verified consistency numerically by checking spatial convergence in Example 1 and Example 2 for manufactured smooth solutions, observing the predicted rates k+1 in the  $L^2$  norm and k in the  $\|\cdot\|_{\omega}$  norm, respectively–consistent with a convergent scheme under mesh refinement. In addition, for this time-dependent heterogeneous-diffusion test, we track the discrete residual at fixed h=1/32 and  $\Delta t=10^{-1}$ . As shown in Figure 14, the residual decreases steadily for both  $\alpha=0.5$  and  $\alpha=0.1$ , confirming convergence toward the steady state.

Figure 15 shows how varying diffusion heterogeneity, with  $\alpha = 0.1$  (moderate) and  $\alpha = 0.01$  (pronounced), affects the solution profile along x = 0.5 and alters the peak value of the solution. The time evolution across various spatial resolutions confirms convergence to the steady-state for different polynomial degrees. The solution profile is well captured, particularly near x = 0.5.

In the second part, we focus on the optimal control framework outlined in Subsection 4. We now apply exactly the same WG discretization and time stepping, with a piecewise-constant diffusion over the ER subdomains, which is estimated from fluorescence-loss data via the PDE-constrained optimization in Subsection 4. This provides a direct continuity from the previous model problem to the biological application. Concretely,  $(\Omega_m, \Omega_b, \Omega_r)$  play the role of the two-and-one subdomains in the 1D test, with  $\omega$  piecewise constant and discontinuous only across known interfaces (the bud neck), so that no change to the numerical scheme is required—only the geometry and data-driven parameters differ. The ER geometry  $\Omega$  is reconstructed from confocal fluorescence microscopy images of cells expressing the ER-luminal marker GFP-HDEL [44]. The ER volume



**Figure 14.** Residual decay for time-dependent heterogeneous diffusion with  $\alpha=0.5$  (a) and  $\alpha=0.1$  (b). Parameters: h=1/32 and  $\Delta t=10^{-1}$ . The residual shown is the discrete  $\ell^2$ -norm, plotted versus the time iterations (log scale on the *y*-axis)



**Figure 15.** Steady-state computed vs. exact solution against mesh resolutions for varying polynomial degrees and heterogeneity parameters:  $\alpha = 0.1$  (top),  $\alpha = 0.01$  (bottom)

was discretized with a tetrahedral mesh generated via Gmsh's Frontal Delaunay algorithm and then quality-improved with Netgen [51]; see Figure 16.

Confocal image data were acquired at ETH Zurich on a Zeiss LSM 780 (ZEN 2011); see acquisition details in [44]. Fluorescence signals were normalized by total intensity within each cell compartment. They are shown as error bars in Figure 17, representing the standard deviation (SD). Based on this dataset, molecular diffusion is analyzed by tracking fluorescence decay post-bleaching, and optimal diffusion parameters are identified within the framework of Subsection 4. Because measurements are available at a finite set of times with variability across replicates, our quantitative comparison overlays the simulated curves with the experimental mean  $\pm$  SD envelopes at those times. This directly addresses agreement-in-time between model and data.

Consider experiments with photobleaching applied to the bud compartment. The initial control

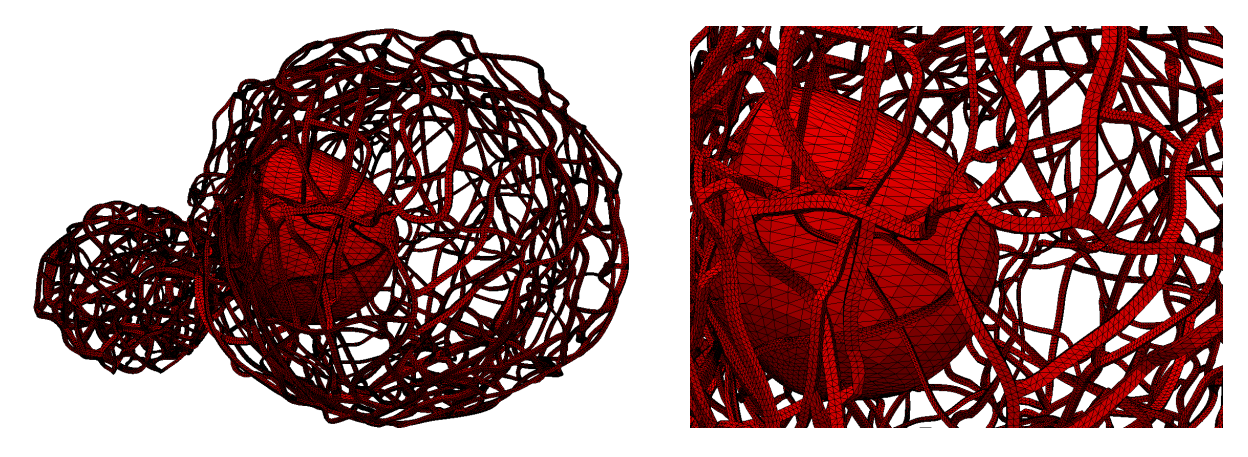


**Figure 16.** Snapshots displaying the volumetric quasi-regular tetrahedral mesh  $\mathcal{M}_h$  of the yeast endoplasmic reticulum. Mesh properties:  $\min_{T \in \mathcal{M}_h} h_T = 5.49 \times 10^{-3}$ ,  $\operatorname{card}(\mathcal{M}_h) = 87,287$ , and 54,537 vertices

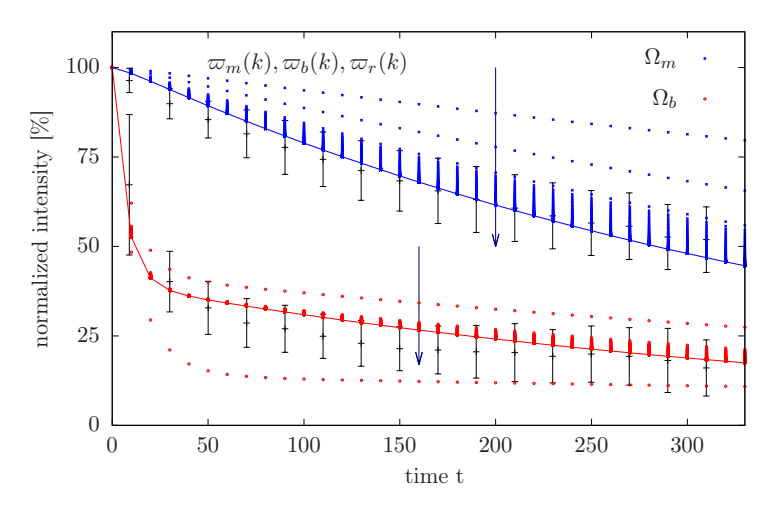


**Figure 17.** Post-photobleaching fluorescence decay in cell compartments during optimal control iterations, showing convergence of the numerical solution as k increases. Error bars show mean  $\pm$  SD from 20 measurements (data from [44])

parameter guesses for the gradient descent algorithm are set as  $\omega_m^0 = 0$ ,  $\omega_b^0 = 2$ , and  $\omega_r^0 = 0.5$ . A resistance value of  $\varepsilon = 10^{-10}$  is imposed, and Tikhonov regularization coefficients  $\delta_i = 1$  are used for all  $i \in \{m, b, r\}$ . The iterative optimal control scheme reaches convergence successfully; see Figure 17, where arrows mark successive iterations and show the simulated fluorescence–decay curves approaching the converged solution (solid line) as the iteration index k increases. Figure 18 displays the normalized objective (relative to its initial value) versus iteration, with an initial steep decline and subsequent flattening, indicating convergence and stabilization of the objective value.

At convergence, the optimal control parameters are  $\omega_m^{\star} = 2.51857$ ,  $\omega_b^{\star} = 2.5186$ , and  $\omega_r^{\star} = 1.0452$ , satisfying  $\omega_m^{\star}/\omega_b^{\star} = 1.000011912$  and  $\omega_m^{\star}/\omega_r^{\star} = 2.41$  (see Figure 19). This suggests that the reporter protein diffuses at similar rates in the mother  $\Omega_m$  and bud  $\Omega_b$ , but significantly slower in the bud-neck  $\Omega_r$ , in line with the experimentally supported diffusion-barrier hypothesis at the neck [43]. Therefore, the reduced value of  $\omega_r^{\star}$  slows fluorescence decay in the unbleached mother compartment.

Using the optimal control parameters at convergence, numerical simulations of fluorescence decay kinetics in the mother and bud domains (Figure 20) closely match experimental data, supporting the heterogeneous-diffusion model on the ER geometry. Quantitatively, the simulated

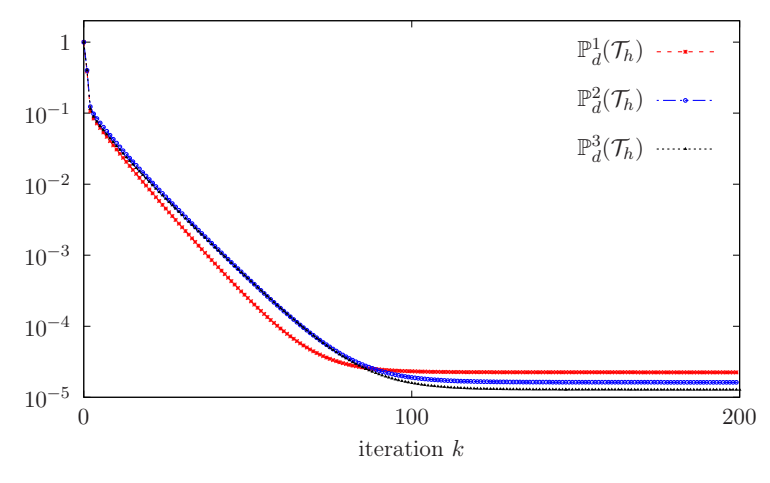


**Figure 18.** Convergence of the normalized cost function vs. optimal-control iteration number (log scale on the y-axis)

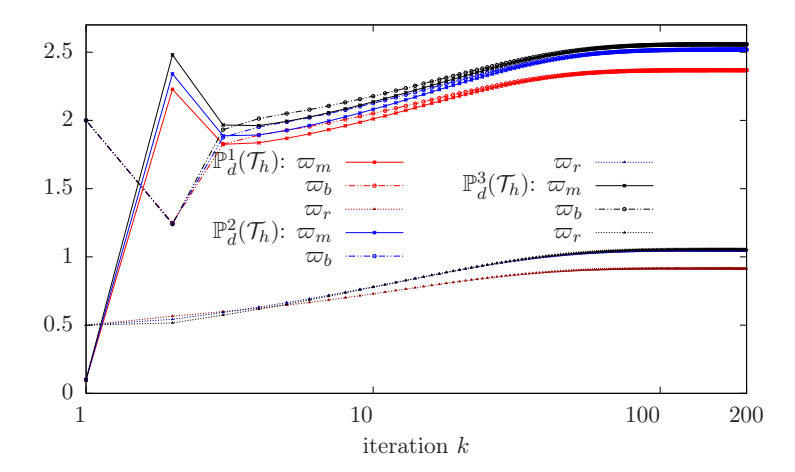


**Figure 19.** Convergence of the heterogeneous diffusion coefficients vs. optimal-control iteration number (log scale on the x-axis) for various polynomial approximations

trajectories lie within (or very near) the mean  $\pm$  SD envelopes at the reported time points in both compartments, consistent with the small misfit values at convergence (Figure 18). Snapshots at selected times are shown in Figure 21.

## Example 6: Steady and time-dependent advection-reaction problems

This example aims to assess the applicability of the introduced weak gradient operator for solving advection–reaction problems, with a view toward multiphase flow modeling; see Subsection 4. A detailed theoretical analysis will be performed in a future separate work.

#### Steady advection-reaction problem

We begin with the steady advection–reaction problem (26). Numerical experiments are performed in 2D with parameters f = 0,  $u_b = 1$ ,  $\mu = 3$ , and  $\beta = (1,0)^T$ . The corresponding solution is  $u(\mathbf{x}) = \exp(-3x)$ .

To assess spatial accuracy, errors are measured against the exact solution on increasingly refined meshes. We test polynomial degrees  $k \in \{1, 2, 4, 6, 8\}$  and report the error  $\|u - u_h\|_{0,\Omega}$ . Table 5 summarizes the error history and shows optimal convergence of order  $\mathcal{O}(h^{k+1})$  for all various

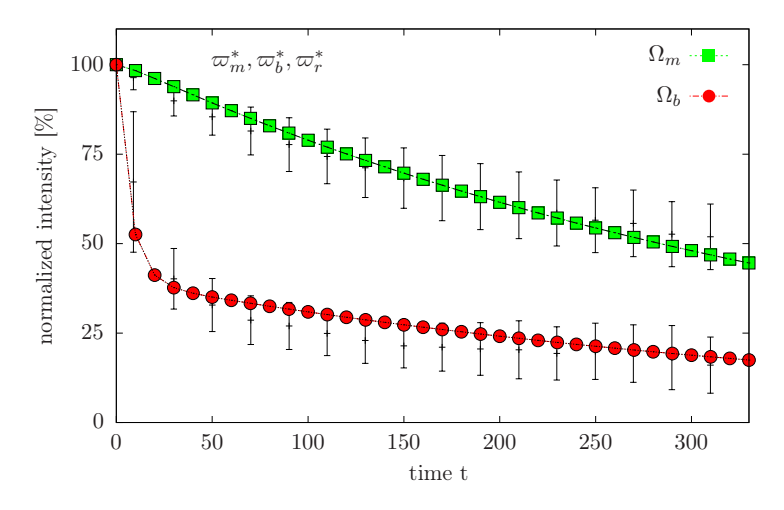


**Figure 20.** Measured vs. simulated fluorescence intensities over time in the cell compartments at convergence. Experimental data are shown with error bars (mean  $\pm$  SD, N=20); simulated curves use the parameters identified by the optimal control framework

**Table 5.** Example 6. Convergence analysis for the advection—reaction problem with different polynomial approximations on triangular meshes

rect of the control of the many of the me actions	0	•	444						
1 2	7	2		4		9		∞	
$\ \epsilon\ _{0,\Omega}$ ROC $\ \epsilon\ _{0,\Omega}$		$\ \epsilon\ _{0,\Omega}$	ROC						
1.129E-2 1.61 5.135E-4	1.61 5.135E-4	5.135E-4	2.89	8.639E-7	4.93	7.568E-10	6.94	3.944E-13	8.89
3.148E-3 1.84 6.483E-5	6.483E-5		2.99	2.699E-8	2.00	5.900E-12	7.00	I	I
8.077E-4 1.96 8.085E-6	8.085E-6		3.00	8.359E-10	5.01	1.290E-13	5.51	I	I
2.038E-4 1.99 1.012E-6		1.012E-6	3.00	2.615E-11	2.00	I	I	I	I
5.100E-5 2.00 1.264E-7		1.264E-7	3.00	8.145E-13	2.00	I	I	I	I
1.276E-5 2.00 1.580E-8	1.580E-8		3.00	I	I	I	I	I	I

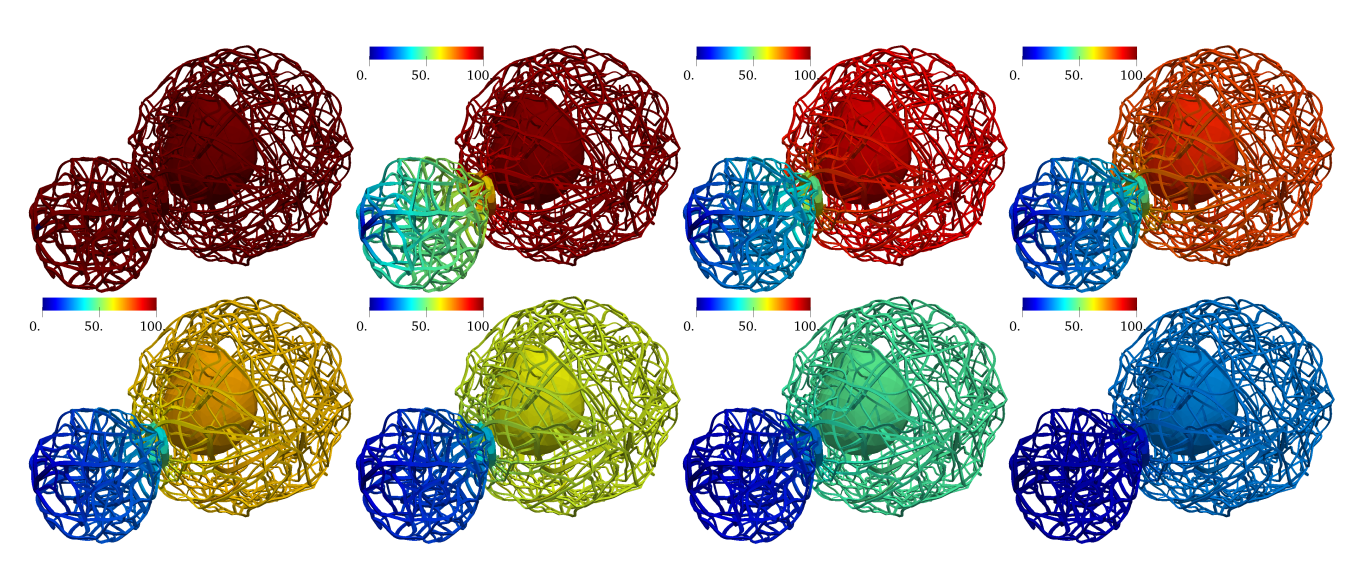


**Figure 21.** Snapshots showing the fluorescence decay in the endoplasmic reticulum following photobleaching applied to the bud and using the optimal heterogeneous diffusion coefficients obtained by optimal control, successively at times  $t \in \{0, 15, 60, 105, 195, 155, 405, 720\}$  and  $u_h \in \mathbb{P}^1_d(\mathcal{M}_h)$ 

degrees.

## Unsteady level-set problem

We consider the 3D Zalesak slotted-disk rotation benchmark with period  $T=4\pi$ . The disk has center at (0.5, 0.75, 0.5), with radius 0.15, slot of depth 0.25 and width 0.05. We prescribe the velocity field

$$\boldsymbol{\beta}(\mathbf{x}) = \left(\left(\frac{1}{2} - y\right)/2, \left(x - \frac{1}{2}\right)/2, 0\right)^{\mathsf{T}}, \quad \text{in } \Omega.$$

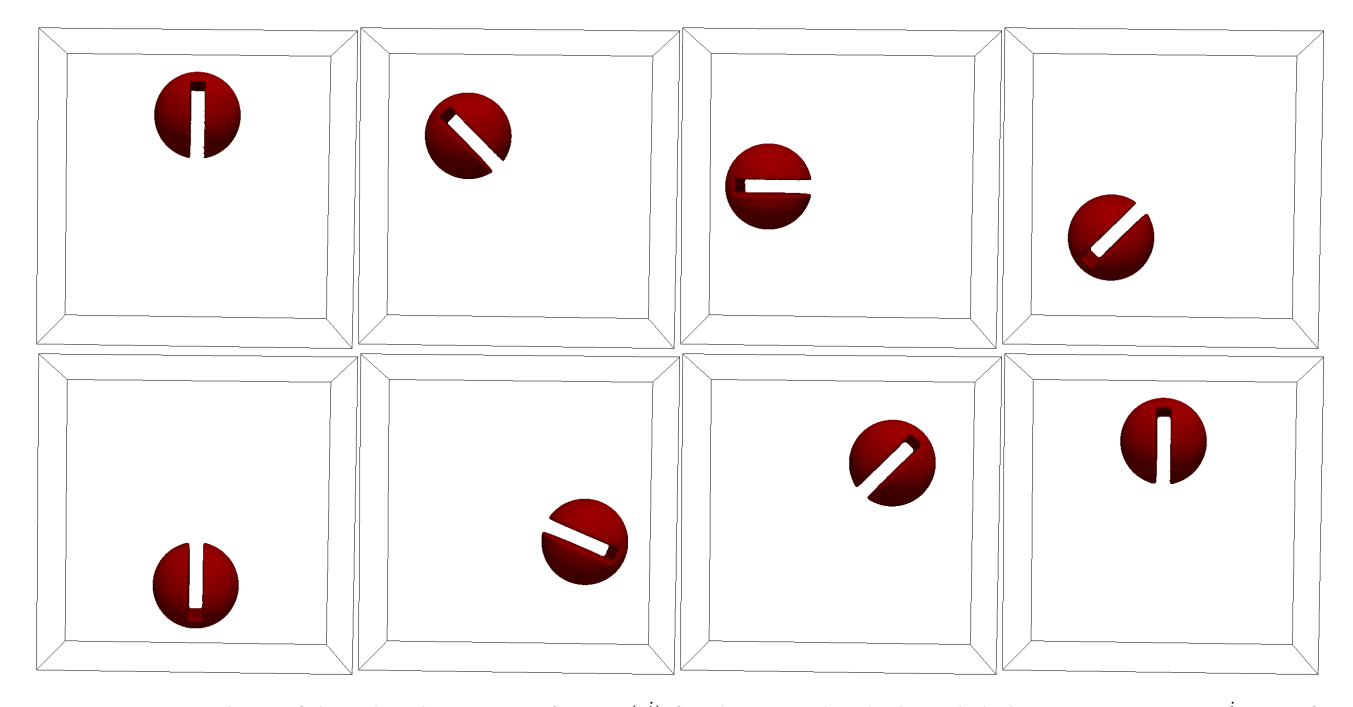


**Figure 22.** Snapshots of the 0-level–set isosurface  $\mathcal{I}_h(t^i)$  for the 3D Zalesak slotted-disk rotation at times  $t^i = j\pi/2$  with j = 0, 1, 2, 3, 4, 5.5, 7, 8 and  $\varphi_h \in \mathbb{P}^1_d(\mathcal{M}_h)$ 

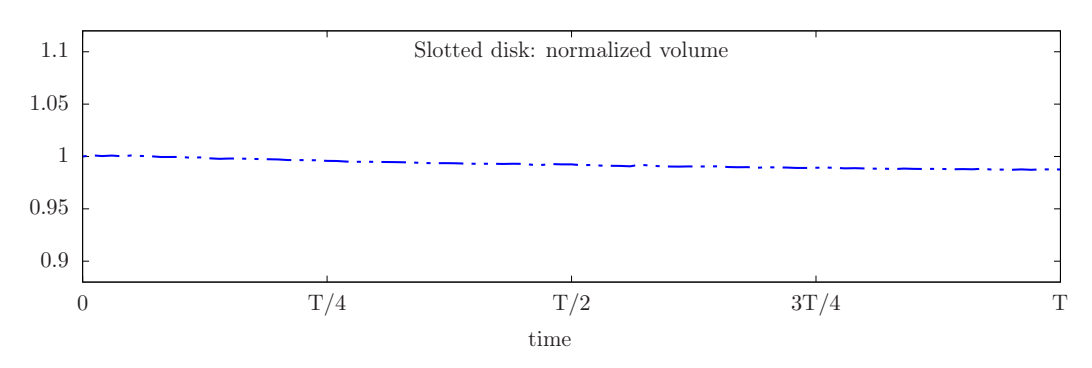


Figure 23. Time history of the normalized enclosed volume of the Zalesak disk over one full rotation

A relatively coarse unstructured tetrahedral mesh of  $\Omega$  is used, with average size h=1/65. We use a time step  $\Delta t=\pi/1000$ . The simulation is run in parallel on 48 cores to assess accuracy over one full rotation. We do not perform re-distancing of  $\varphi$ ; see, e.g., [49]. Figure 22 shows the zero level–set isosurface at selected times, indicating good volume preservation and sharp-feature transport. Figure 23 reports the normalized volume (relative to its initial value) versus time, showing good mass preservation with an error below 1% throughout the simulation period.

## 6 Conclusions

This study introduces a high-order weak discontinuous finite element approach for addressing one-, two- and three-dimensional problems. A single stabilizer is incorporated into our definition of the weak gradient, ensuring consistency and discrete stability and yielding a well-posed scheme. The method demonstrates optimal convergence, with theoretical estimates provided in the norms  $\|.\|_{U}$  and  $L^2$ .

The method is extended to address a range of problems, starting with time-dependent heterogeneous diffusion and progressing to a biophysically relevant model of protein mobility in the endoplasmic reticulum within the realistic geometry of a budding yeast cell. To showcase its versatility, we also present preliminary numerical results for advection–reaction problems. Numerical tests confirm the validity of the theoretical error analysis in 1D, 2D, and 3D settings, demonstrating optimal error convergence rates for various unstructured quasi-uniform meshes and high-order polynomial approximations.

The principal contributions of this work are as follows:

- We devised a weak discontinuous Galerkin scheme for elliptic problems that incorporates a
  novel weak gradient operator. Theoretical analysis proves that the associated discrete bilinear
  form satisfies consistency and stability, ensuring well-posedness. Error bounds are established
  in various norms.
- Numerical experiments in 1D, 2D, and 3D, using high-order approximation spaces, verify the optimal theoretical rates predicted by the analysis.
- The method extends naturally to unsteady diffusion with heterogeneous coefficients. Validation against exact solutions demonstrates robustness, particularly in cases with strong heterogeneity and derivative jumps.
- Within an optimal-control framework, we modeled compartmentalized diffusion in the endoplasmic reticulum of a budding yeast cell using data and a realistic cell geometry, capturing mobility restrictions induced by spatially varying diffusivity.
- Within multiphase flow modeling, the discrete weak gradient operator is employed for both steady advection–reaction and time-dependent level–set problems. Preliminary numerical results reveal promising performance in terms of mass conservation and stability.

#### Limitations

The proposed method is promising but was developed and analyzed primarily for second-order elliptic problems; the advection-reaction case was illustrated only through preliminary tests. A comprehensive extension to multiphase-flow settings remains to be carried out.

Future work will focus on extending the presented approach to nonlinear interfacial flows [52– 54], Eulerian fluid–structure interactions [55, 56], and multiphysics modeling [57, 58], areas in which discontinuous Galerkin methods have demonstrated advantages over standard Galerkin formulations, particularly with respect to mass conservation.

#### **Declarations**

#### Use of AI tools

The author declares that he has not used Artificial Intelligence (AI) tools in the creation of this article.

## Data availability statement

No Data associated with the manuscript.

## **Ethical approval (optional)**

The author states that this research adheres to the ethical standards. This research does not involve either human participants or animals.

## **Consent for publication**

Not applicable

#### **Conflicts of interest**

The author declares that he has no conflict of interest.

## **Funding**

No funding was received for this research.

#### Author's contributions

The author confirms being the sole contributor of this work and approves it for publication.

#### Acknowledgements

Not applicable

## References

- [1] Rivière, B. Discontinuous Galerkin Methods for Solving Elliptic and Parabolic Equations: Theory and Implementation. Society for Industrial and Applied Mathematics: United States of America, (2008).
- [2] Di Pietro, D.A. and Ern, A. Mathematical Aspects of Discontinuous Galerkin Methods (Vol. 69). Springer: Heidelberg, (2011). [CrossRef]
- [3] Feng, X., Karakashian, O. and Xing, Y. Recent Developments in Discontinuous Galerkin Finite Element Methods for Partial Differential Equations: 2012 John H Barrett Memorial Lectures. Springer Cham: Heidelberg, (2014). [CrossRef]

- [4] Bertoluzza, S., Guidoboni, G., Hild, R., Prada, D., Prud'homme, C., Sacco, R. et al. A HDG method for elliptic problems with integral boundary condition: Theory and Applications. *Journal of Scientific Computing*, 95, 6, (2023). [CrossRef]
- [5] Song, L. and Zhang, Z. Superconvergence property of an over-penalized discontinuous Galerkin finite element gradient recovery method. *Journal of Computational Physics*, 299, 1004-1020, (2015). [CrossRef]
- [6] Dong, Z. Discontinuous Galerkin methods for the biharmonic problem on polygonal and polyhedral meshes. *ArXiv Preprint*, *ArXiv:1807.07817*, (2018). [CrossRef]
- [7] Ta, M., Pigeonneau, F. and Saramito, P. An implicit high order discontinuous Galerkin level set method for two-phase flow problems. In Proceedings, *ICMF-2016 9th International Conference on Multiphase Flow*, pp. 1-7, Florence, Italy, (2016, May).
- [8] Jaśkowiec, J. and Sukumar, N. Penalty-free discontinuous Galerkin method. *International Journal for Numerical Methods in Engineering*, 125(12), e7472, (2024). [CrossRef]
- [9] Li, R., Gao, Y. and Chen, Z. Adaptive discontinuous Galerkin finite element methods for the Allen-Cahn equation on polygonal meshes. *Numerical Algorithms*, 95, 1981-2014, (2024). [CrossRef]
- [10] Wang, J. and Ye, X. A weak Galerkin mixed finite element method for second order elliptic problems. *Mathematics of Computation*, 83, 2101-2126, (2014). [CrossRef]
- [11] Nguyen, N.C., Peraire, J. and Cockburn, B. A class of embedded discontinuous Galerkin methods for computational fluid dynamics. *Journal of Computational Physics*, 302, 674-692, (2015). [CrossRef]
- [12] Pigeonneau, F., Hachem, E. and Saramito, P. Discontinuous Galerkin finite element method applied to the coupled unsteady Stokes/Cahn-Hilliard equations. *International Journal for Numerical Methods in Fluids*, 90(6), 267-295, (2019). [CrossRef]
- [13] Badrkhani, V., ten Eikelder, M.F., Hiemstra, R.R. and Schillinger, D. The matrix-free macroelement Hybridized discontinuous Galerkin method for steady and unsteady compressible flows. *International Journal for Numerical Methods in Fluids*, 97(4), 462-483, (2025). [CrossRef]
- [14] Riviere, B., Shaw, S. and Whiteman, J.R. Discontinuous Galerkin finite element methods for dynamic linear solid viscoelasticity problems. *Numerical Methods for Partial Differential Equations: An International Journal*, 23(5), 1149-1166, (2007). [CrossRef]
- [15] Saramito, P. and Wachs, A. Progress in numerical simulation of yield stress fluid flows. *Rheologica Acta*, 56, 211-230, (2017). [CrossRef]
- [16] Jang, Y. and Shaw, S. Discontinuous Galerkin finite element method for dynamic viscoelasticity models of power-law type. *Numerical Methods for Partial Differential Equations*, 40(6), e23107, (2024). [CrossRef]
- [17] Pelties, C., De la Puente, J., Ampuero, J.P., Brietzke, G.B. and Käser, M. Three-dimensional dynamic rupture simulation with a high-order discontinuous Galerkin method on unstructured tetrahedral meshes. *Journal of Geophysical Research: Solid Earth*, 117(B2), 1-15, (2012). [CrossRef]
- [18] Antonietti, P.F., Facciolà, C., Houston, P., Mazzieri, I., Pennesi, G. and Verani, M. High–order discontinuous Galerkin methods on polyhedral grids for geophysical applications: seismic wave propagation and fractured reservoir simulations. In, *Polyhedral Methods in Geosciences* (pp. 159–225). SEMA SIMAI Springer Series, Cham, Germany: Springer, (2021). [CrossRef]
- [19] Antonietti, P.F., Facciola, C., Russo, A. and Verani, M. Discontinuous Galerkin approximation

- of flows in fractured porous media on polytopic grids. SIAM Journal on Scientific Computing, 41(1), A109-A138, (2019). [CrossRef]
- [20] Shu, C.W. Discontinuous Galerkin methods: general approach and stability. Numerical Solutions of Partial Differential Equations, 201, 149-201, (2009).
- [21] Shu, C.W. Discontinuous Galerkin methods for time-dependent convection dominated problems: basics, recent developments and comparison with other methods. In, Building Bridges: Connections and Challenges in Modern Approaches to Numerical Partial Differential Equations (pp. 371-399). Lecture Notes in Computational Science and Engineering, Cham, Germany: Springer, (2016). [CrossRef]
- [22] Wang, X., Malluwawadu, N.S., Gao, F. and McMillan, T.C. A modified weak Galerkin finite element method. Journal of Computational and Applied Mathematics, 271, 319-327, (2014). [CrossRef]
- [23] Gao, F., Ye, X. and Zhang, S. A discontinuous Galerkin finite element method without interior penalty terms. Advances in Applied Mathematics and Mechanics, 14(2), 299-314, (2022). [CrossRef]
- [24] Chen, G. and Xie, X. A robust weak Galerkin finite element method for linear elasticity with strong symmetric stresses. Computational Methods in Applied Mathematics, 16(3), 389-408, (2016). [CrossRef]
- [25] Falk, R.S. Nonconforming finite element methods for the equations of linear elasticity. *Mathe*matics of Computation, 57(196), 529-550, (1991).
- [26] Hansbo, A. and Hansbo, P. A finite element method for the simulation of strong and weak discontinuities in solid mechanics. Computer Methods in Applied Mechanics and Engineering, 193(33-35), 3523-3540, (2004). [CrossRef]
- [27] Guo, R., Lin, T. and Lin, Y. Error estimates for a partially penalized immersed finite element method for elasticity interface problems. ESAIM: Mathematical Modelling and Numerical Analysis, 54(1), 1-24, (2020). [CrossRef]
- [28] Zhai, Q., Xie, H., Zhang, R. and Zhang, Z. The weak Galerkin method for elliptic eigenvalue problems. Communications in Computational Physics, 26(1), 160-191, (2019). [CrossRef]
- [29] Mu, L., Wang, J. and Ye, X. Effective implementation of the weak Galerkin finite element methods for the biharmonic equation. Computers & Mathematics with Applications, 74(6), 1215-1222, (2017). [CrossRef]
- [30] Cui, M., Ye, X. and Zhang, S. A modified weak Galerkin finite element method for the biharmonic equation on polytopal meshes. Communications on Applied Mathematics and Computation, 3, 91-105, (2021). [CrossRef]
- [31] Mu, L., Wang, J. and Ye, X. A stable numerical algorithm for the Brinkman equations by weak Galerkin finite element methods. *Journal of Computational Physics*, 273, 327-342, (2014). CrossRef
- [32] Zhu, H., Zou, Y., Chai, S. and Zhou, C. A weak Galerkin method with RT elements for a stochastic parabolic differential equation. East Asian Journal on Applied Mathematics, 9(4), 818-830, (2019). [CrossRef]
- [33] Wang, C. New discretization schemes for time-harmonic Maxwell equations by weak Galerkin finite element methods. *Journal of Computational and Applied Mathematics*, 341, 127-143, (2018). [CrossRef]
- [34] Mu, L. Weak Galerkin based a posteriori error estimates for second order elliptic interface

- problems on polygonal meshes. Journal of Computational and Applied Mathematics, 361, 413-425, (2019). [CrossRef]
- [35] Dehghan, M. and Gharibi, Z. Optimal convergence analysis of the energy-preserving immersed weak Galerkin method for second-order hyperbolic interface problems in inhomogeneous media. Computers & Mathematics with Applications, 105, 150-171, (2022). [CrossRef]
- [36] Mu, L., Wang, J., Wang, Y. and Ye, X. Interior penalty discontinuous Galerkin method on very general polygonal and polyhedral meshes. Journal of Computational and Applied Mathematics, 255, 432-440, (2014). [CrossRef]
- [37] Ye, X. and Zhang, S. A conforming discontinuous Galerkin finite element method: Part II. *ArXiv Preprint, ArXiv:1907.01397, (2019).* [CrossRef]
- [38] Hristov, J. A non-linear diffusion problem with power-law diffusivity: An approximate solution experimenting with a modified sinc function. Mathematical Modelling and Numerical Simulation with Applications, 4(5), 6-44, (2024). [CrossRef]
- [39] Ciarlet, P.G. The Finite Element Method for Elliptic Problems (Vol. 40). Society for Industrial and Applied Mathematics: United States of Amerika, (2002). [CrossRef]
- [40] Di Pietro, D.A. and Droniou, J.  $W^{s,p}$ -approximation properties of elliptic projectors on polynomial spaces, with application to the error analysis of a Hybrid High-Order discretisation of Leray-Lions problems. Mathematical Models and Methods in Applied Sciences, 27(05), 879-908, (2017). [CrossRef]
- [41] Aubin, J.P. Analyse fonctionnelle appliquée. Presses universitaires de France: France, (1987).
- [42] Laadhari, A. Implicit finite element methodology for the numerical modeling of incompressible two-fluid flows with moving hyperelastic interface. Applied Mathematics and Computation, 333, 376-400, (2018). [CrossRef]
- [43] Luedeke, C., Frei, S.B., Sbalzarini, I., Schwarz, H., Spang, A. and Barral, Y. Septin-dependent compartmentalization of the endoplasmic reticulum during yeast polarized growth. The Journal of Cell Biology, 169(6), 897-908, (2005). [CrossRef]
- [44] Laadhari, A., Barral, Y. and Székely, G. A data-driven optimal control method for endoplasmic reticulum membrane compartmentalization in budding yeast cells. Mathematical Methods in the Applied Sciences, 46(8), 8855-8876, (2023). [CrossRef]
- [45] Lee, Z.Y., Prouteau, M., Gotta, M. and Barral, Y. Compartmentalization of the endoplasmic reticulum in the early C. elegans embryos. Journal of Cell Biology, 214(6), 665-676, (2016). CrossRef
- [46] Janela, J., Lefebvre, A. and Maury, B. A penalty method for the simulation of fluid-rigid body interaction. ESAIM: Proceedings, 14, 115-123, (2005). [CrossRef]
- [47] Laadhari, A. Exact Newton method with third-order convergence to model the dynamics of bubbles in incompressible flow. Applied Mathematics Letters, 69, 138-145, (2017). [CrossRef]
- [48] Laadhari, A., Saramito, P., Misbah, C. and Székely, G. Fully implicit methodology for the dynamics of biomembranes and capillary interfaces by combining the level set and Newton methods. Journal of Computational Physics, 343, 271-299, (2017). [CrossRef]
- [49] Laadhari, A., Saramito, P. and Misbah, C. Improving the mass conservation of the level set method in a finite element context. Comptes Rendus. Comptes Rendus. Mathématique, 348(9-10), 535-540, (2010). [CrossRef]
- [50] Efficient C++ finite element computing with Rheolef, CNRS-CCSD, (2024). www-ljk.imag.

### fr/membres/Pierre.Saramito/rheolef, [Accessed: 01.09.2024]

- [51] Geuzaine, C., Remacle, J.F. and Dular, P. Gmsh: a three-dimensional finite element mesh generator. International Journal for Numerical Methods in Engineering, 79(11), 1309-1331, (2009).
- [52] Laadhari, A. and Quarteroni, A. Numerical modeling of heart valves using resistive Eulerian surfaces. International Journal for Numerical Methods in Biomedical Engineering, 32(5), e02743, (2016). [CrossRef]
- [53] Caboussat, A., Picasso, M. and Rappaz, J. Numerical simulation of free surface incompressible liquid flows surrounded by compressible gas. Journal of Computational Physics, 203(2), 626-649, (2005). [CrossRef]
- [54] Doyeux, V., Guyot, Y., Chabannes, V., Prud'Homme, C. and Ismail, M. Simulation of two-fluid flows using a finite element/level set method. Application to bubbles and vesicle dynamics. Journal of Computational and Applied Mathematics, 246, 251-259, (2013). [CrossRef]
- [55] Laadhari, A. An operator splitting strategy for fluid-structure interaction problems with thin elastic structures in an incompressible Newtonian flow. Applied Mathematics Letters, 81, 35-43, (2018). [CrossRef]
- [56] Griffith, B.E. Immersed boundary model of aortic heart valve dynamics with physiological driving and loading conditions. International Journal for Numerical Methods in Biomedical Engineering, 28(3), 317-345, (2012). [CrossRef]
- [57] Kolahdouz, E.M. and Salac, D. A numerical model for the trans-membrane voltage of vesicles. Applied Mathematics Letters, 39, 7-12, (2015). [CrossRef]
- [58] Barrett, J.W., Garcke, H. and Nürnberg, R. Numerical computations of the dynamics of fluidic membranes and vesicles. *Physical Review E*, 92(5), 052704, (2015). [CrossRef]

Mathematical Modelling and Numerical Simulation with Applications (MMNSA) (https://mmnsa.researchcommons.org)



**Copyright:** © 2025 by the authors. This work is licensed under a Creative Commons Attribution 4.0 (CC BY) International License. The authors retain ownership of the copyright for their article, but they allow anyone to download, reuse, reprint, modify, distribute, and/or copy articles in MMNSA, so long as the original authors and source are credited. To see the complete license contents, please visit (http://creativecommons.org/licenses/by/4.0/).

How to cite this article: Laadhari, A. (2025). Stabilized weak-gradient discontinuous finite elements with optimal error estimates for second-order elliptic PDEs. Mathematical Modelling and Numerical Simulation with Applications, 5(3), 644-680. https://doi.org/10.53391/2791-8564.1007